THE UNIVERSITY OF CALGARY

ANTICOINCIDENCE GAMMA RAY SPECTROMETRY OF GEOLOGICAL SAMPLES

by

JON D. CANADAY

A THESIS

SUBMITTED TO THE FACULTY OF GRADUATE STUDIES

IN PARTIAL FULFILLMENT OF THE REQUIREMENTS FOR

THE DEGREE OF MASTER OF SCIENCE

DEPARTMENT OF PHYSICS

CALGARY, ALBERTA

MARCH, 1975

THE UNIVERSITY OF CALGARY

FACULTY OF GRADUATE STUDIES

The undersigned certify that they have read and recommend to the Faculty of Graduate Studies for acceptance a thesis entitled "Anticoincidence Gamma Ray Spectrometry of Geological Samples," submitted by Jon D. Canaday in partial fulfillment of the requirements for the degree of Master of Science.

C J Bland.

Dr. C.J. Bland (Supervisor)
Department of Physics

H Roy Krouse

Dr. H.R. Krouse
Department of Physics

Dr. H.W. Jones
Department of Physics

March 25, 1975
(date)

R. Bruce Farquharson

Dr. R.B. Farquharson
Department of Geology

ABSTRACT

When measuring low concentrations of the radioactive elements K^{40}, U^{238} and Th^{232} with a NaI(Tl) detector in the 0.1 to 3 MeV range, it is essential that the background contribution to the gamma-ray spectrum be minimized. Background radiation resulting from environmental sources and from the soft component of the cosmic flux has been reduced from 2×10^4 counts per minute to 1204 ± 4 c.p.m. by 12 cm. of iron shielding surrounding the detector. This rate was further reduced by a liquid scintillator of 3 cm. thickness which subtends a solid angle of approximately 2π steradians with respect to the detector. The liquid scintillator, connected in anticoincidence with the detector, further reduced the background rate to 1037 ± 4 c.p.m. This decrease when compared to the liquid scintillator photon detection efficiency indicates that the background radiation results from low energy photons which are produced by the interaction of cosmic ray muons and nucleons with the iron shield. A liquid scintillation thickness of 20 cm. would significantly reduce this remaining background.

The spectrometer is nearly linear over the 0.1 to 3 MeV range and has sufficient energy resolution to separate the higher absolute-intensity photopeaks of K^{40}, U^{238}, and Th^{232}. The instrument is stable to within 2 channels for at least 15 hours, a period exceeding the optimum counting time of 4 hours for 1 kg. samples.

The increase in the ratio of total (sample plus background) to background counts for the measured photopeaks is 2.5% when the anticoincidence system is used. Assigning a 2σ detection limit, the

limits for the measured samples are 0.18×10^{-3} gm./gm., 0.6×10^{-7} gm./gm., and 0.38×10^{-6} gm./gm. for K^{40}, U^{238}, and Th^{232} respectively.

ACKNOWLEDGEMENTS

At the suggestion of my supervisor, Dr. C.J. Bland, whose direction is gratefully acknowledged, this research was initiated. Dr. T. Mathews, Dr. C.Y. Kim and Mr. A. Knudsen generously loaned equipment. Appreciation is also extended to Mr. P. Siska and Mr. E. Zimmer for advice with the electronics and to Mrs. V. Matwick for skillful typing. Mr. J. Steeples and the staff of the machine shop provided assistance with the design and installation of the equipment.

I am indebted to the University for the award of Graduate Assistantships and a grant towards computing costs. Some equipment and summer stipends were provided by an operating grant from the National Research Council.

TABLE OF CONTENTS

CHAPTER		PAGE
	ABSTRACT	iii
	ACKNOWLEDGEMENTS	v
	TABLE OF CONTENTS	vi
	LIST OF TABLES	viii
	LIST OF FIGURES	ix
	INTRODUCTION	1
1.	SODIUM IODIDE DETECTOR	
	1.1 Introduction	2
	1.2 Absorption of Gamma Ray Photons	3
	1.3 Scintillation Process	9
	1.4 Photomultiplication	12
	1.5 Calibration of the Detector	14
	1.6 Efficiency of the Detector	22
2.	BACKGROUND RADIATION AND SHIELDING	
	2.1 Introduction	34
	2.2 Radioactive Contamination Sources of Background	34
	2.3 Cosmic Radiation Sources of Background	42
	2.4 Shielding	51
3.	LIQUID SCINTILLATOR	
	3.1 Introduction	61
	3.2 Mechanism of Liquid Scintillation	61

TABLE OF CONTENTS (cont'd)

CHAPTER		PAGE
	3.3 Description of the Liquid Scintillator	63
	3.4 Efficiency of the Liquid Scintillator	63
4.	THE COMPLETE SPECTROMETER	
	4.1 Introduction	67
	4.2 Anticoincidence Circuit Logic	69
	4.3 Electronics	69
	4.4 Optimization of the Spectrometer	74
	4.5 Conclusions	75
5.	GAMMA RAY SPECTROMETRY OF SAMPLES	
	5.1 Introduction	80
	5.2 Spectrometry of Geological Samples	80
	5.3 Analysis of the Spectra	89
	5.4 Counting Errors, Anticoincidence System Effectiveness, Optimum Analysis Time, and Detection Limits . . .	99
	5.5 Summary and Final Conclusions	105
	REFERENCES	108
	APPENDICES	
	I. Computer Program for Concentration Calculations	112
	II. Results of the Computer Program for the GCOS 1300-2 sample	117

LIST OF TABLES

TABLE		PAGE
1-1	Energy calibration standards	15
1-2	Detection efficiencies, D(E), for r_o = 2 in., t_o = 4 in., R = 3/4r	28
1-3	Detection efficiencies, I(E), for r_0 = 2 in., t_o = 4 in., R = 3/4r	32
2-1	Natural radioisotope concentrations in various materials	41
2-2	Chemical composition of primary cosmic rays	43
2-3	Collision mean free path of the nucleonic component in various materials	57
3-1	Liquid scintillator characteristics	64
4-1	Anticoincidence circuit truth table	70
4-2	Background counting rates	77
5-1	Radioactive constants of K^{40}	84
5-2	Decay series of Th^{232}	86
5-3	Decay series of U^{238}	88
5-4	Comparison of photopeak parameters	96
5-5	Sample concentration correction factors	98
5-6	Concentrations of GCOS samples	100
5-7	Effect of the anticoincidence system in reducing photopeak background	104

LIST OF FIGURES

FIGURE		PAGE
1-1	Linear absorption coefficient for NaI(TL)	5
1-2	Schematic energy diagram of a luminescence centre . . .	11
1-3	Wiring diagram of photomultiplier base	16
1-4	Spectrometer energy calibration	17
1-5	Spectrometer stability	18
1-6	Photopeak energy resolution	20
1-7	Peak-to-total ratio for a 4 in. x 4 in. NaI(Tl) crystal	23
1-8	Intrinsic efficiency of a 4 in. x 4 in. NaI(Tl) crystal for source distances in cm. on axis of detector . .	24
1-9	Geometry of a disk source and cylindrical detector . .	27
1-10	K^{39} concentration for samples of various thickness . .	31
2-1	Mass absorption coefficients for high-Z materials . . .	38
2-2	Mass absorption coefficients for low-Z materials . . .	39
2-3	Components of the cosmic radiation in the atmosphere .	47
2-4	Omnidirectional differential energy spectrom of muons and nucleons near sea level	48
2-5	Probable energy loss of muons in 1.51 cm. of NaI(Tl)	50
2-6	Omnidirectional integral energy spectrum of the electrons and photons near sea level	52
2-7	Range-energy relation for muons	54
2-8	Energy spectra of photons emitted after capture of thermal neutrons in various shielding materials . .	59
3-1	Photon detection efficiency of the liquid scintillator	66
4-1	Schematic diagram of the spectrometer	68

LIST OF FIGURES (cont'd)

FIGURE		PAGE
4-2	Block diagram of the electronics	71
4-3	Emitter follower circuit	73
4-4	Effect of delay time on efficiency and background . . .	76
4-5	Effect of anticoincidence system on background spectrum	78
5-1	Decay scheme of K^{40}	83
5-2	Decay series of the Th^{232} series	85
5-3	Decay series of the U^{238} series	87
5-4	Spectrum of GCOS 1300-2 sample	90
5-5	Schematic diagram of a photopeak	93
5-6	Net counting rates of photopeaks	94
5-7	Effect of counting time on sample per cent error . . .	103

INTRODUCTION

An understanding of the geochemistry of the radioactive elements potassium, uranium, and thorium requires analysis of very low concentrations of their isotopes and decay products. This objective necessitates the development of sensitive instrumentation and digital output data in a convenient form. The analysis of such data is given in Chapter 5. The alternatives for increasing the spectrometer sensitivity include placing the instrument underground to reduce the cosmic ray contribution to the background spectrum, the use of massive shielding surrounding the NaI(Tl) detector, and connecting the detector in anticoincidence with a second detector so that pulses coincident with both devices are not analyzed. The anticoincidence system used is described in Chapter 4.

A cost-effective choice for the anticoincidence detector must be made and will depend on the type of background radiation which is to be reduced and on the spectral energy range. Chapter 3 presents the evaluation of the effectiveness of the liquid scintillator used for this purpose. In Chapter 2, an analysis of the sources of background radiation and of the shielding designed to decrease this flux is made.

In addition to the instrumentation objectives of sensitivity and digital data, sufficient spectrometer energy resolution and stability are also required. These properties are determined primarily by the NaI(Tl) detector and photomultiplier, as seen in Chapter 1. This analysis begins with the processes of gamma-ray absorption of source photons by the NaI(Tl) detector and the subsequent scintillation mechanism.

CHAPTER 1

SODIUM IODIDE DETECTOR

1.1 Introduction

A gamma photon, of energy E, expends part or all of its energy when passing through the NaI(Tl) scintillation detector. The energy expended by the photon in the scintillator is transformed into a voltage output pulse by the following successive steps:

(1) the photon transfers an amount of its energy E_1, ($E_1 < E$) to a charged particle, usually an electron by the photo-electric effect, Compton effect, or alternatively creates an electron-positron pair;

(2) the electron dissipates a fraction of its energy AE_1, ($A \leq 1$) in the scintillator by excitation or ionization of the NaI(Tl) molecules;

(3) the energy AE_1 is converted into p visible photons with an average energy E_p, by the de-excitation or de-ionization of the detector molecules with a conversion efficiency

$$Y = pE_p/AE_1 \qquad (1\text{-}1)$$

which is 13% for NaI(Tl);

(4) A fraction of the visible photons, K, goes toward the photocathode of the photomultiplier; also, because of the imperfect transmission J ($J < 1$) of the crystal to its own fluorescence radiation, a fraction of the visible photons, J, will be absorbed by the crystal itself;

(5) the visible photons reaching the photocathode are converted into photoelectrons with an efficiency L (L = number of photoelectrons per visible photon).

Thus, the total number of photoelectrons, n, produced at the photocathode as a result of the detection of a gamma photon of energy E is

$$n = \frac{(AE_1)(Y)(KJ)(L)}{E_p} \qquad (1\text{-}2)$$

The photoelectrons at the photocathode are then multiplied by the photomultiplier tube; if G is the amplification of the tube, the total charge at the final collector plate (anode) is

$$Q_a = nGe \qquad (1\text{-}3)$$

where e is the charge of the electron. The proportionality between E_1 and Q_a allows the scintillator to be used as a spectrometer in the ideal case. Reference to Figure (1-4) indicates that this ideal linearity is not quite attained in practice.

1.2 Absorption of Gamma Ray Photons

Gamma ray photons are absorbed in the sodium iodide crystal primarily by the processes of (1) the photoelectric effect, (2) Compton scattering, and (3) pair production. As each photon is removed from the incident photon beam of intensity, I, in a single event, the fraction removed, ΔI, is proportional to the thickness of crystal traversed, Δd, so that

$$\frac{\Delta I}{I} = -\alpha \Delta d \qquad (1\text{-}4)$$

where α is the linear attenuation coefficient in cm^{-1}. If the incident photon beam and the crystal are homogeneous, α is constant and integration gives

$$I = I_o e^{-\alpha d} . \tag{1-5}$$

Because each of these absorption processes occurs independently, the total attenuation coefficient is the linear sum of the coefficients for each process

$$\alpha = \alpha_{ph} + \alpha_c + \alpha_{pp} . \tag{1-6}$$

The absorption processes further depend on the photon energy of the incident beam and on the composition of the absorber. For a sodium iodide-thallium activated crystal, the linear absorption coefficient as a function of incident photon energy is shown in Figure (1-1). These interactions can also be written in terms of the mass attenuation coefficient which is independent of absorber density as

$$\frac{\alpha}{\rho} = \frac{\alpha_{ph} + \alpha_c + \alpha_{pp}}{\rho} , \quad (cm^2\ g^{-1}) \tag{1-7}$$

where ρ is the density and in terms of the cross-section per atom

$$a^{\alpha} = a^{\alpha}_{ph} + a^{\alpha}_{c} + a^{\alpha}_{pp}, \quad (cm^2\ atom^{-1}) . \tag{1-8}$$

If N is Avogadro's number and A the atomic weight of the absorber, then

$$a^{\alpha} = \frac{A}{N}\frac{\alpha}{\rho} . \tag{1-9}$$

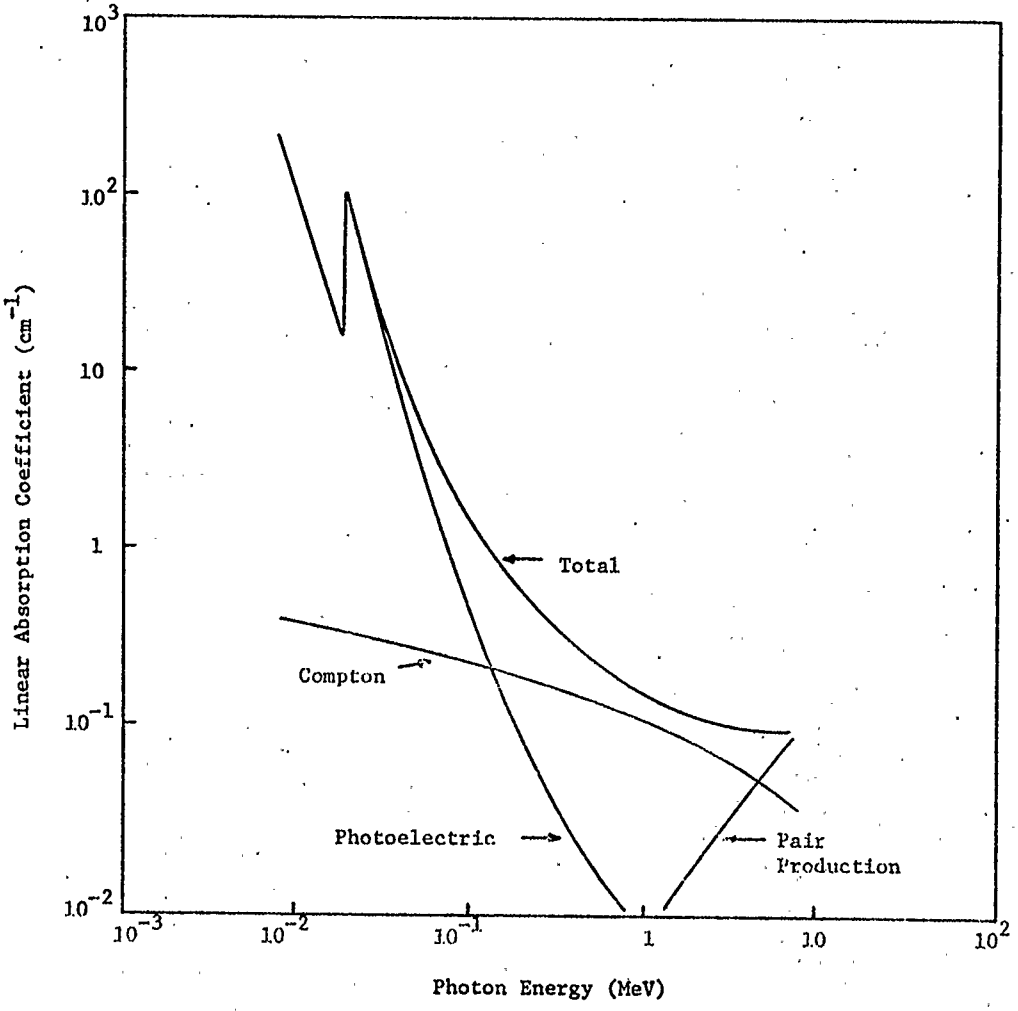

FIGURE (1-1) Linear absorption coefficient for NaI(Tl). (From Adams and Gasparini, 1970).

Each of these processes will now be discussed in somewhat more detail.

In the photoelectric absorption process, the incident photon of energy, $h\nu$, transfers all of its energy to a bound electron in the absorber which is ejected from the atom with a kinetic energy

$$T = h\nu - E_b \tag{1-10}$$

where E_b is the binding energy of the electron. Total absorption of the photon energy can occur only if the electron is initially bound to the atom, because a third body, the nucleus, is necessary for momentum conservation. Furthermore, for the photoelectric interaction to occur, the energy of the incident photons must exceed the electron binding energy.

The electron binding energy leads to a discontinuity in the photoelectric interaction probability at energies equal to the binding energies of the K-, L-, or M- shell electrons for the sodium iodide crystal. When energetically possible, approximately 80% of the interactions occur in the K-shell, and a large fraction of the remaining 20% occur in the L-shell.

The Compton effect results when a gamma photon of the incident beam collides with a free or loosely bound outer electron of the crystal. In contrast to the photoelectric effect, the incident photon transfers only a fraction of its energy, $h\nu$, and is deflected from its original direction by an angle, ϕ, with a lower energy, $h\nu'$. When the conservation of linear momentum and energy is considered for the relativistic case, the interaction is given by (Arya, 1966)

$$h\nu' = \frac{h\nu}{1 + \frac{h\nu}{m_o c^2}(1 - \cos\phi)} \qquad (1\text{-}11)$$

where $m_o c^2$ is the rest energy of the electron, 0.511 MeV. The energy of the scattered photon decreases with increasing ϕ to a minimum value occurring when $\phi = \pi$, i.e., when the photon is backscattered. Equation (1-11) then becomes

$$h\nu' = \frac{h\nu}{1 + 2\frac{h\nu}{m_o c^2}} \qquad (1\text{-}12)$$

or

$$h\nu' = \frac{m_o c^2}{2} \quad \frac{1}{1 + \frac{m_o c^2}{2h\nu}} \qquad (1\text{-}13)$$

For incident gamma-ray energies of $h\nu > \frac{1}{2} m_o c^2$, the maximum energy of the scattered photons approaches

$$h\nu' = \frac{m_o c^2}{2} = 0.255 \text{ MeV} . \qquad (1\text{-}14)$$

Thus, spectra of high energy photons may show a back-scattering peak near 0.255 MeV caused by Compton scattering in the surrounding shielding material.

The angle of emission of the electron, θ, is related to the photon scattering angle, ϕ, by the equation

$$\cot\theta = \left(1 + \frac{h\nu}{m_o c^2}\right) \tan(\phi/2) . \qquad (1\text{-}15)$$

The kinetic energy of the scattered electron, T, is the difference between the original photon energy, $h\nu$, and the scattered photon energy, $h\nu'$,

$$T = \frac{\frac{(h\nu)^2}{m_o c^2}(1 - \cos\phi)}{1 + \frac{h\nu}{m_o c^2}(1 - \cos\phi)} \tag{1-16}$$

Equations (1-15) and (1-16) indicate that the energy of the scattered electron ranges from zero at $\phi = 0$, $\Theta = \pi/2$ to a maximum value at $\phi = \pi$, $\theta = 0$. The maximum value is known as the Compton edge energy and is given by

$$T_m = \frac{h\nu}{1 + \frac{1}{2}\frac{m_o c^2}{h\nu}} \tag{1-17}$$

The sum of the energies due to the photon back-scattering peak and the electron Compton edge gives the energy of the original gamma photon.

When the incident photon energy is above $2m_o c^2 = 1.022$ MeV, the photon loses its energy through the process of electron-positron pair formation. Conservation of linear momentum requires the presence of a heavy body; pair production occurs in the field of the nucleus and conservation of energy gives

$$h\nu = 2m_o c^2 + T_- + T_+ + T_{nuc} \tag{1-18}$$

where $h\nu$ is the energy of the incident photon, $2m_o c^2$ is the rest energy of the electron-positron pair; T_-, T_+, and T_{nuc} are the

kinetic energies of the electron, positron, and nucleus respectively. Because of the large mass of the nucleus, it acquires only a small amount of kinetic energy, and T_{nuc} may be neglected.

1.3 Scintillation Process

The detector electrons, having absorbed gamma photons, now dissipate their energy by excitation or ionization of the crystal molecules. Subsequent de-excitation and de-ionization produces fluorescent radiation. Block (1928) introduced the energy band model for perfect crystals in which the electronic energy states of an isolated atom or molecule consist of a series of discrete levels defined by the Schrödinger equation. In an inorganic crystal lattice the electronic energy levels of the outer electrons are perturbed by interactions between the atoms or ions and are broadened into a series of continuous allowed energy bands, separated by forbidden regions of energy. The highest filled band, the valence band, is separated from the lowest empty band, the conduction band, by an energy difference of a few eV. Electrons in the valence band may be raised into the conduction band by the absorption of quanta leaving positive holes in the valence band. Photoconduction can then occur due to the independent motion of the electrons in the conduction band and of the holes in the valence band. Alternatively, the excited electron may remain bound to the positive hole forming an exciton, whose energy band lies below the conduction band.

This energy band model applies only to structures having a perfect crystal lattice. Varaitions in energy bands due to lattice

defects and impurities such as thallium produce local electronic energy levels in the normally forbidden region between the conduction and valence bands. Stated differently, when the perfect periodicity of the lattice is disturbed, it becomes possible for electrons to acquire energies which are forbidden in the perfect crystal. These additional energy levels are localized at the crystal defect unlike the energy bands themselves which extend throughout the crystal. Unoccupied, these defects may serve as orbits for electrons moving to the conduction or to the exciton bands. These centres can be classified as follows (Birks, 1964):

(a) Luminescence centers in which the de-excitation produces a radiative transition.

(b) Quenching centers in which the absorbed quanta are dissipated thermally without radiation.

(c) Traps, having metastable levels from which the electrons or excitons may subsequently return to the conduction band by acquiring thermal energy from lattice vibrations or fall to the valence band by a radiationless transition.

The conditions for luminescence emission and quenching of a center can be described qualitatively in terms of a model introduced by von Hippel (1936) and applied to luminescence by Seitz (1938). This model is general and is applicable to all luminescent materials including organic molecules. The model is presented schematically in Figure (1-2) in which the abscissa is a configuration coordinate specifying the configurations of the ions around the center. The ordinate is the potential energy of the ground, E_o, and excited, E_1, electronic states of the

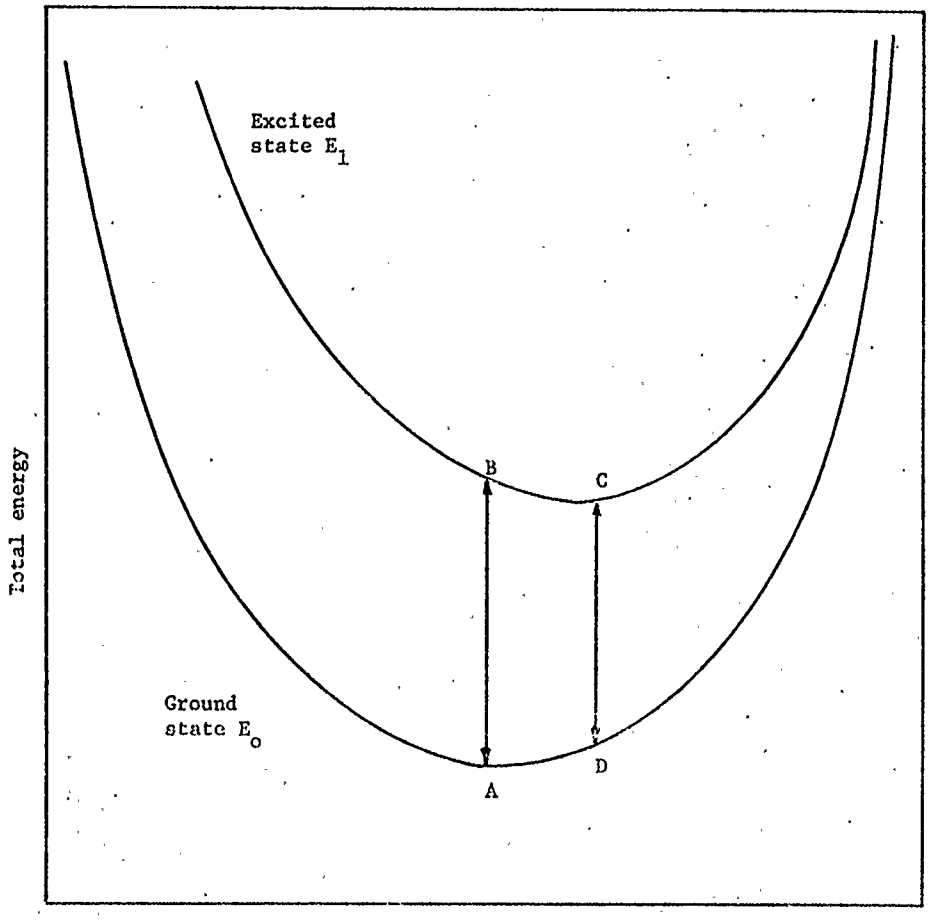

FIGURE (1-2) Schematic energy diagram of a luminescence centre.

luminescence centre. The equilibrium positions of the ground and excited state correspond to points A and C.

The absorption of a photon, $h\nu$, by the centre, or its excitation by the capture of an exciton, causes a transition from the ground to the excited state of the system. Such a transition occurs along a vertical line, AB, since the electron transitions involved in emission or absorption occur in a time interval smaller than that for atomic or ionic motions. Immediately following this transition the system is not in a state of minimum potential energy, and thus it moves from B to C. The time spent at C depends on the probability of the optical transition, CD, which produces the luminescence emission $h\nu'$. After this transition, the centre, now in its ground state, returns from D to A with thermal dissipation of excess vibrational energy. The energy of the emitted photon, $h\nu'$, is smaller than that of the absorbed photon, $h\nu$, by the amount of energy transferred to lattice vibrations.

1.4 Photomultiplication

Photons produced by the scintillation process have a typical wavelength of 4200Å in NaI(Tl). The photomultiplier used, whose cathode spectral response matches the scintillation emission spectrum, is an EMI 9732 tube containing an S-11 (Cs_3Sb-O) cathode with a peak response at 3900Å and ten CsSb dynodes. The quantum efficiency of the cathode, that is the number of photoelectrons emitted per incident scintillation photon, is 19%.

The electron gain is given ideally by

$$G = \delta^m \qquad (1\text{-}19)$$

where δ is the average secondary emission coefficient, and m is the number of dynodes. However, this expression takes no account of the fact that the K-D1 collection efficiency, f, will be less than 100%, as will the transfer efficiency of electrons between dynodes, g, although g is nearly 100%. A more realistic expression for the gain is therefore

$$G = f(g\delta)^m . \tag{1-20}$$

Typical values of f are 90%, and values of $g\delta \simeq 4.5$ at moderate operating voltages are obtainable. An empirical relation for δ when CsSb dynodes are used is

$$\delta = 0.2\ (V_s)^{0.7} \tag{1-21}$$

where V_s is the interdynode voltage. In this spectrometer, $V_s \simeq 70$ volts, resulting in a gain of 9.8×10^5. The overall voltage, V, is approximately proportional to V_s, so that substitution of (1-21) into (1-20) and differentiation gives

$$\frac{dG}{G} = 0.7\ m\ \frac{dV}{V} . \tag{1-22}$$

For most photomultipliers, 0.7 m is nearly 10. Thus, as a rough guide, the stability of the power supply should be an order of magnitude better than that specified for the application. In order to obtain a ± 1 channel stability when using a 400 channel analyzer, dG/G is $\pm 2.5 \times 10^{-3}$ and dV/V is $\pm 2.5 \times 10^{-4}$. The stability of the Fluke 412B power supply is specified as one part in 10^4 per 24 hours. This value was not directly confirmed; however, the

stability of the total spectrometer has been evaluated and is discussed in Section 1.5. The wiring diagram of the photomultiplier base is shown in Figure (1-3).

1.5 Calibration of the Detector

Energy calibration requires examining the dependence of the pulse height, measured in terms of the analyzer channel number, on the photon energy of the source. In general, the relationship is nearly linear with a somewhat larger slope for higher energy photons and major deviations from linearity below 0.1 MeV. This calibration is performed by plotting the channel number of the full energy peak versus the known photon energy. Table (1-1) lists the calibration standards and Figure (1-4) shows the relation between photon energy and analyzer channel. It is usually necessary to perform such a calibration each time a sample is analysed in order to determine whether any instrumental drift has occurred.

It is essential that the spectrometer remain stable during the period of analysis, that is, the photopeaks should appear in the same set of channels. This stability is necessary in order that the background spectrum can be subtracted from the sample spectrum where computer methods using a preset number of channels are applied. Possible sources of instrumental drift are the high voltage supply, the photomultiplier, and the multichannel analyzer. The Fluke 412B is reported to be stable to one part in 10^4 per 24 hours, while the Laben 400 channel analyzer has a drift of one channel per 24 hours.

TABLE (1-1)

Energy Calibration Standards

Isotope	Half-life (Yr.)	Gamma-ray energy (MeV)	Absolute Intensity (%)
Na^{22}	2.60	0.511 1.275	178
Cs^{137}	30.00	0.662	85
Mn^{54}	0.83	0.835	100
Y^{88}	0.28	0.898 1.836	91 100
Co^{60}	5.26	1.17 1.33	100 100
K^{40}	1.30×10^9	1.46	11
Th^{232} (Tl^{208})	3.10 min.	2.62	100

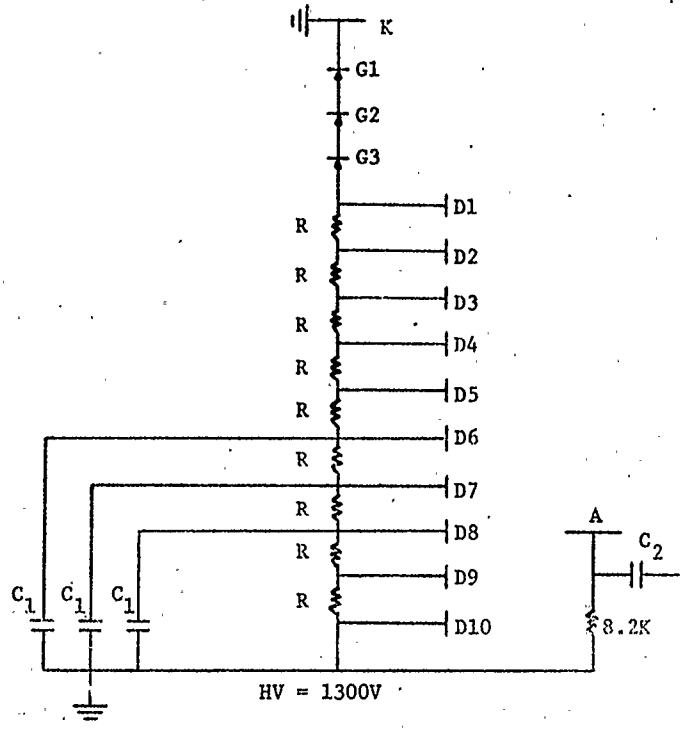

FIGURE (1-3) Wiring diagram of photomultiplier base
R = 220 KΩ, C_1 = 0.01μF, C_2 = 3KV, 0.01μF.

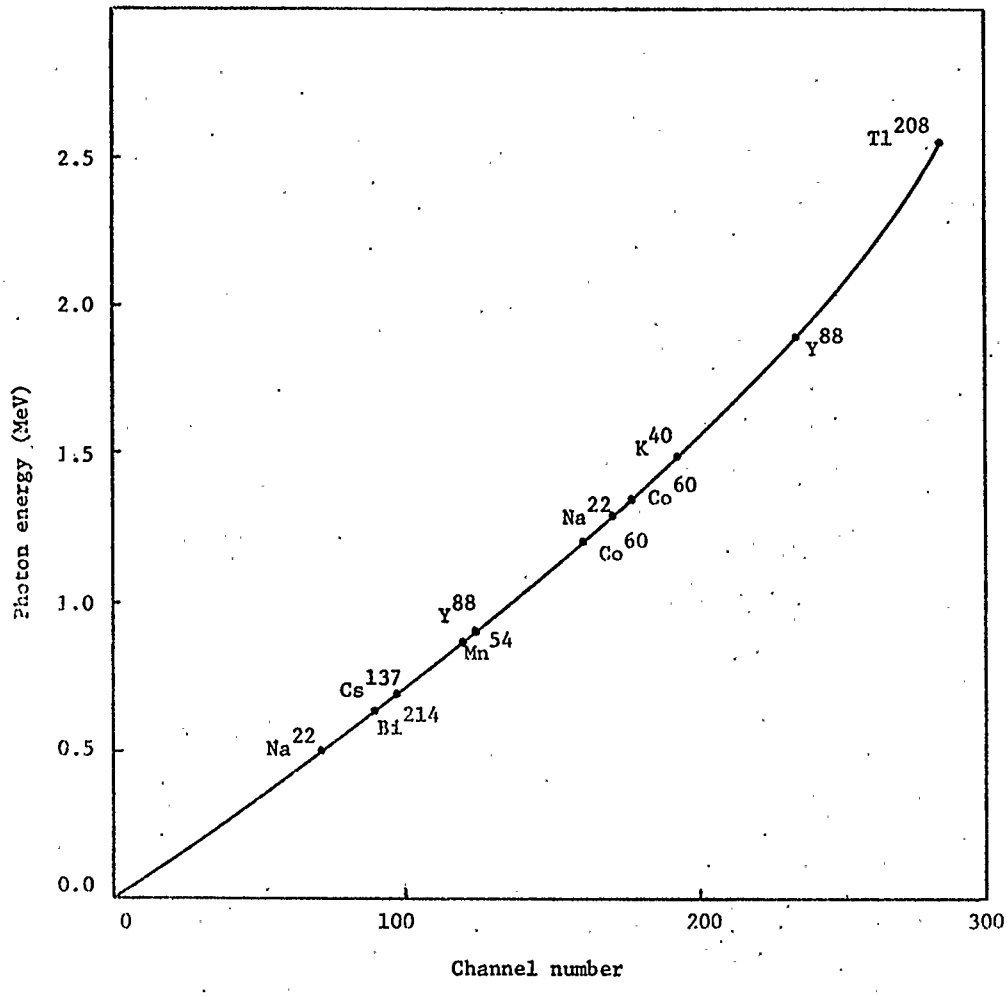

FIGURE (1-4) Spectrometer energy calibration.

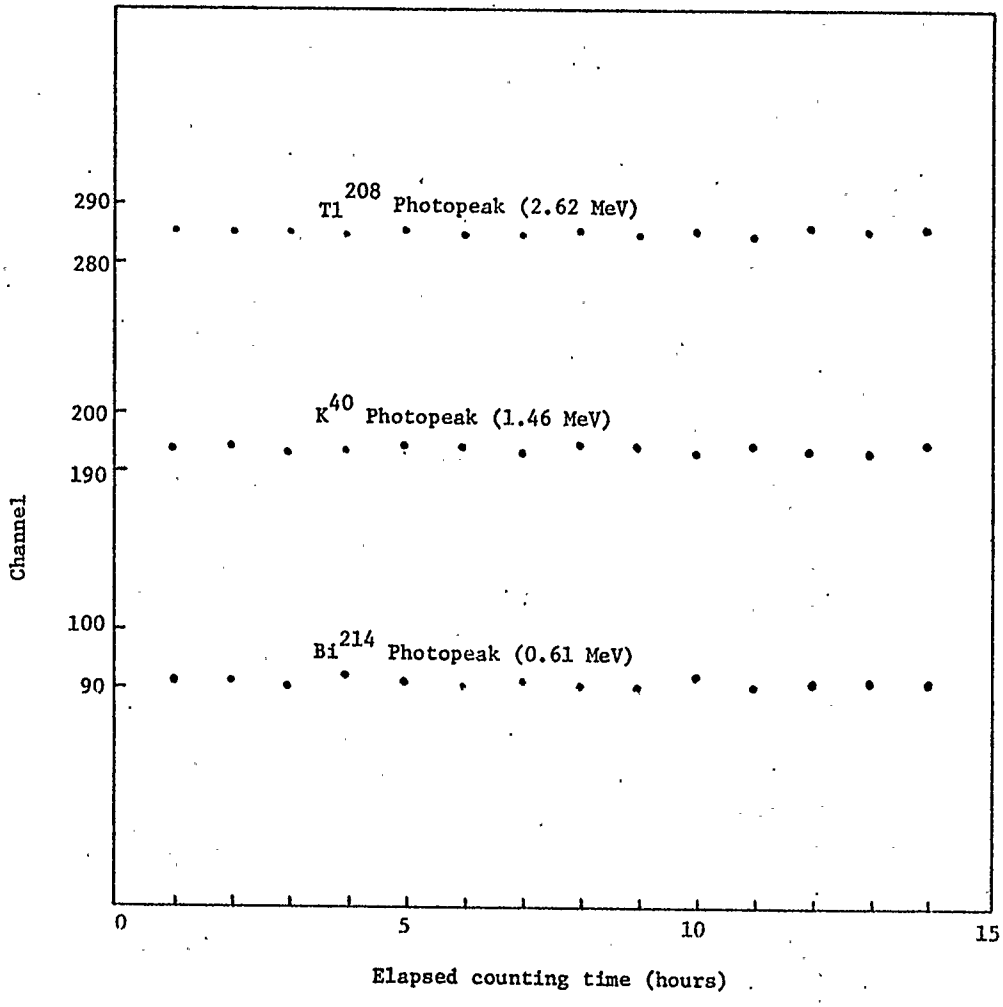

FIGURE (1-5) Spectrometer stability.

The most serious source of drift is caused by the photomultiplier due to voltage instability and cathode aging. The overall stability was determined by monitoring the sample photopeaks of K^{40}, U^{238}, and Th^{232} over a relatively extended period. The maximum drift is about two channels over 15 hours as shown in Figure (1-5).

The next instrumental parameter to be evaluated is the energy resolution. Equation (1-2) shows that the factors affecting the number of electrons collected at the photocathode are the fraction of the energy dissipated by the electrons AE_1, the conversion efficiency Y, the transmission of the crystal to its fluorescence radiation J, and the fraction of visible photons reaching the cathode. Fluctuation in these parameters will result in a spread of n, and will therefore affect the resolution. The resolution is primarily dependent on the presence of inhomogeneities, variations of light reflections and imperfections in the crystal. Because the number of fluoresence photons produced in the crystal is proportional to the energy that the incident photon has deposited in the crystal, the statistical variation is higher for the lower-energy incident photons. Figure (1-6) illustrates the affect of incident photon energy on resolution where $R_1 = \Delta E/E$.

Assuming all of the gamma photon energy is dissipated in the crystal, the number of visible scintillation photons can be calculated from Equation (1-1) as

$$p = \frac{Yh\nu}{E_p} \qquad (1\text{-}23)$$

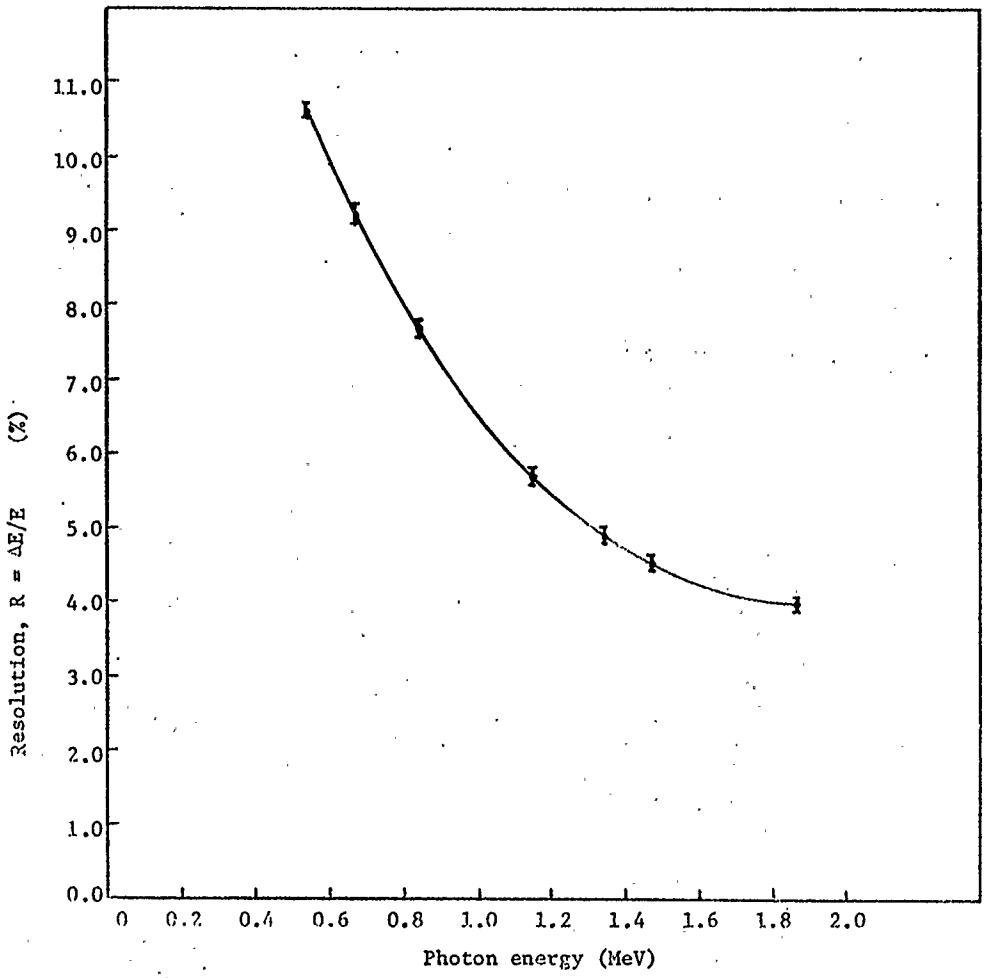

FIGURE (1-6) Photopeak energy resolution.

which is 2.8×10^4 for a Cs^{137} source with $h\nu = 0.662$ MeV. The standard deviation of p is

$$\sigma_p = p^{\frac{1}{2}} \tag{1-24}$$

and the FWHM of the photopeak is

$$R' = 2.36 \frac{\sigma_p}{p} h\nu = 9.2 \times 10^3 \text{ eV} \tag{1-25}$$

The energy resolution when considering only the scintillation processes is

$$R_S = \frac{R'}{h\nu} = 1.4\% \tag{1-26}$$

The variance in the photomultiplication process can be evaluated by first noting that the number of photoelectrons produced at the cathode is, assuming J = 1, K = 1 in Eq. (1-2),

$$n = Lp \tag{1-27}$$

where L is the cathode quantum efficiency, 19%. For a Cs^{137} source $n = 5.6 \times 10^3$. If all the dynodes exhibit the same secondary emission factor, δ, the variance of the photomultiplier gain is (Kowalski, 1970)

$$\left(\frac{\sigma_v}{V_o}\right)^2 = \frac{1}{n} \frac{\delta}{\delta-1} \tag{1-28}$$

and the resolution (FWHM) is

$$R_p = 2.36 \frac{\sigma_v}{V_o} = 3.6\% \tag{1-29}$$

The total calculated resolution due to scintillation and photomultiplication is

$$R_{total} = \left(R_S^2 + R_P^2\right)^{\frac{1}{2}} = 3.9\% \quad . \tag{1-30}$$

From Figure (1-6) it is seen that the actual resolution at 0.662 MeV is 9%. This indicates that the assumptions concerning the conversion of gamma photons into visible photons, the transmission of these visible photons in the crystal, and the uniformity of the dynode multiplication are not strictly valid. Because of the high transmission by NaI(Tl) of scintillation photons and because of the Al_2O_3 reflective coating, J and K will be nearly unity. Thus, the majority of the variance appears to be caused by a non-uniform dynode chain.

1.6 Efficiency of the Detector

The intrinsic efficiency of the detector is the fraction of monochromatic isotropic radiation of photon energy, E, incident on the detector surface which interacts with the crystal to produce a measurable scintillation. For a point source emitting s photons per unit time, the intrinsic efficiency is given (Adams and Gasparini, 1970) by

$$\varepsilon = \frac{k}{\omega s} \tag{1-31}$$

where k is the number of counts per unit time over the whole spectrum; ω is the ratio of the solid angle subtended by the detector to the

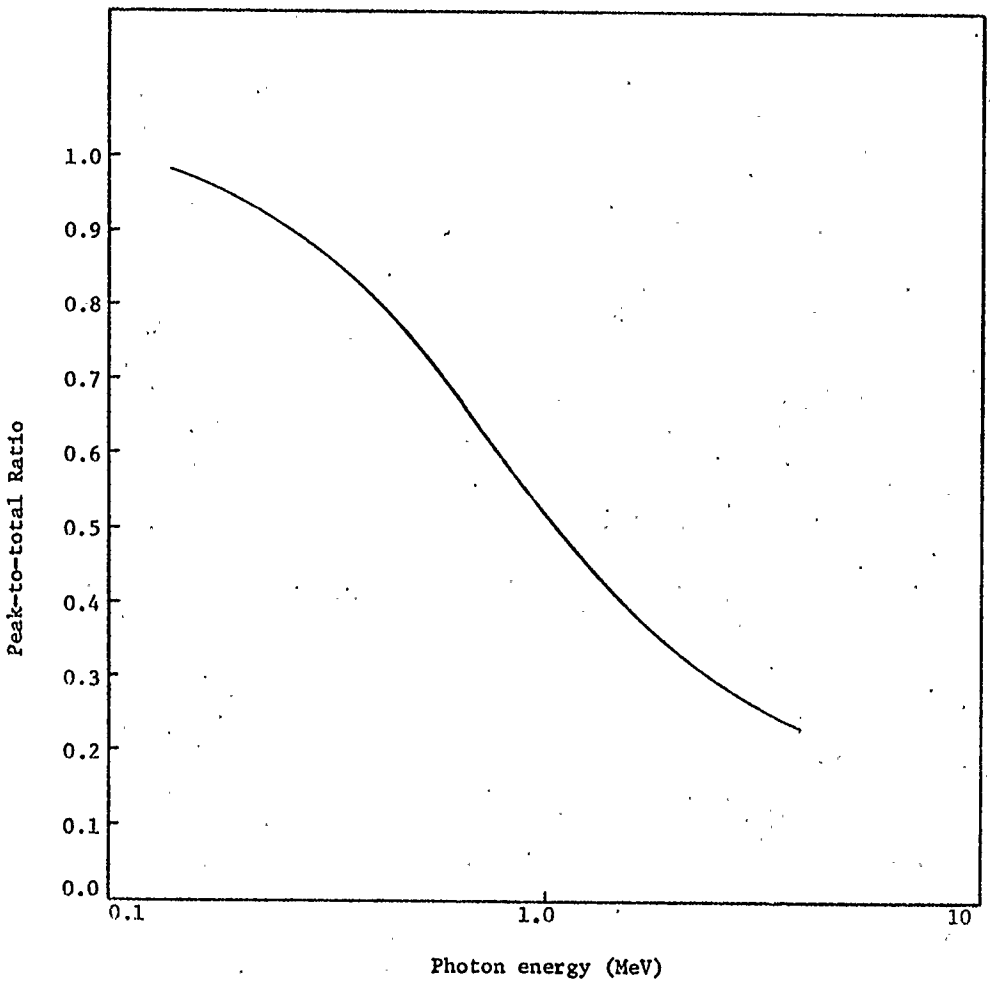

FIGURE (1-7) Peak-to-total ratio for a 4 in. x 4 in. NaI(Tl) crystal. (From Heath, 1964).

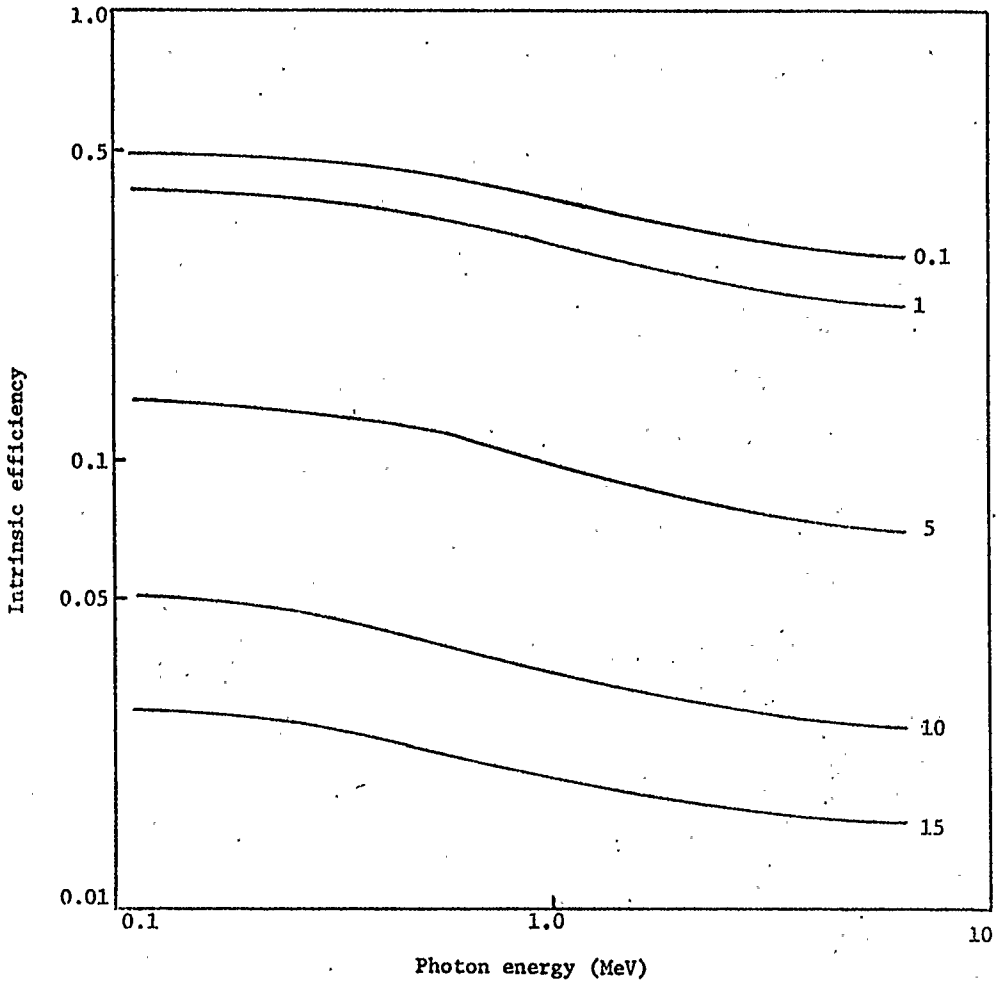

FIGURE (1-8) Intrinsic efficiency of a 4 in. x 4 in. NaI(Tl) crystal for source distances in cm. on axis of detector. (From Heath, 1964).

solid angle of a sphere, 4π sr. When the full energy peak is considered, the number of counts per unit time, k_F, is

$$\varepsilon = \frac{k_F}{\omega s P} \qquad (1\text{-}32)$$

where P is the photofraction, i.e., the ratio of the number of counts in the full energy peak to the number of counts in the total spectrum. The energy dependence of the peak-to-total ratio and of the intrinsic efficiency for the 4 in. x 4 in. NaI(Tl) detector are shown in Figures (1-7) and (1-8).

Intrinsic efficiencies have been calculated for point sources, circular disk sources, and line sources but not for cylindrical sources such as the geological samples measured in this experiment. It thus becomes necessary to determine the efficiency for counting a cylindrical source; this parameter will be referred to as the geometrical efficiency. First, however, it is necessary to define the detection efficiency.

The detection efficiency, D(E), is the fraction of gamma photons emitted from the source which interact with the detector and lose a measurable amount of energy. This quantity can be calculated for known values of the absorption cross section, α, for sodium iodide when the source-detector geometry is well defined. An equation for the evaluation of D(E) has been derived (Heath, 1964) for the case of a disk source whose centre is located on the axis of a right circular cylindrical detector where the plane of the disk is parallel to the upper surface of the detector and is given by

$$D(E) = \frac{1}{\pi R^2} \int_0^R x\,dx \int_{-\pi/2}^{\pi/2} d\phi \left\{ \int_0^{\tan^{-1}\frac{-x\sin\phi + \sqrt{x^2\sin^2\phi - (x^2 - r_o^2)}}{h_o + t_o}} \left[1 - \varepsilon^{-\tau(E)\left(\frac{t_o}{\cos\theta}\right)}\right] \sin\theta\, d\theta \right.$$

$$\left. + \int_{\tan^{-1}\frac{-x\sin\phi + \sqrt{x^2\sin^2\phi - (x^2 - r_o^2)}}{h_o + t_o}}^{\tan^{-1}\left(\frac{-x\sin\phi + \sqrt{x^2\sin^2\phi - (x^2 - r_o^2)}}{h_o}\right)} \left[1 - e^{-\tau(E)\left(\frac{-x\sin\phi + \sqrt{x^2\sin^2\phi - (x^2 - r_o^2)}}{\sin\theta} - \frac{h_o}{\cos\theta}\right)}\right] \sin\theta\, d\theta \right\} \quad (1\text{-}33)$$

where t_o is the detector thickness, r_o is the detector radius, h_o is the vertical distance between the top surface of the detector and the source, and R is the radius of the disk source. This geometry is illustrated in Figure (1-9).

For the 4 in. x 4 in. sodium iodide detector where r_o = 2 in., t_o = 4 in., and R = 3/4 r_o, values of D(E) have been interpolated for photon energies of 0.61 MeV, 1.46 MeV, and 2.62 MeV as shown in Table (1-2).

Any source-detector configuration enclosed within a shield, for the purpose of reducing the background contribution to the gamma ray spectrum, will result in the detector's analyzing source photons which have been scattering by the shielding. As discussed in Section 1.2, the energy of the scattered photon is less than the photon's original energy, approaching a maximum value of 0.255 MeV. It is, therefore, convenient to work in terms

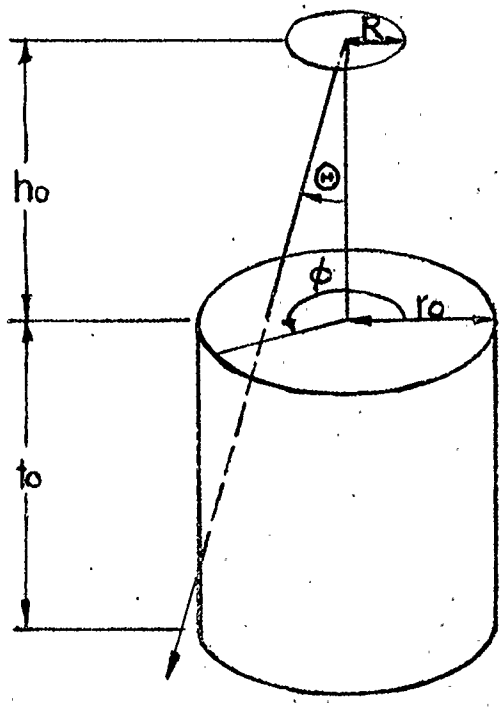

FIGURE (1-9) Geometry of a disk source and cylindrical detector.

TABLE (1-2)

Detection Efficiencies, D(E),

r_o = 2 in., t_o = 4 in., R = 3/4 r_o.

h_o(cm) \ E(MeV)	0.61	1.46	2.62
0.001	0.34393	0.31241	0.22962
1.0	0.19429	0.19732	0.12770
3.0	0.09219	0.10700	0.06114
5.0	0.05297	0.06681	0.03562
10.0	0.02010	0.02822	0.01389
15.0	0.01040	0.01533	0.00731
20.0	0.00632	0.00959	0.00456

of the photopeak efficiency, H(E). This quantity is defined as the probability that a gamma photon of energy E, emitted from the source, will appear in the photopeak of the pulse-height spectrum. The utility of this quantity is that most of the spurious contribution to the spectrum, as produced by scattering, has no effect on the photopeak itself. Therefore, the photopeak represents a more accurate region of the spectrum to measure the emission rate than in regions where scattering must also be accounted for.

Because of the large number of multiple processes occurring in a scintillation detector, it would be difficult to calculate H(E) directly. It is thus convenient to define the relation

$$H(E) = D(E)P \tag{1-34}$$

where D(E) is the detector efficiency and P is the ratio of the number of counts in the photopeak to the total number of counts in the spectrum. The peak-to-total ratio has been determined experimentally under conditions which allow the scattered photons to be neglected. Values of P for a 4 in. x 4 in. sodium iodide detector as a function of photon energy are shown in Figure (1-7).

The emission rate of photons from the source is then given by

$$N_s = \frac{N_p}{D(E)P} \text{ , (counts/sec)} \tag{1-35}$$

where N_p is the number of counts per second of the photopeak. Comparison of Equations (1-32) and (1-35) shows that the intrinsic

efficiency and the detection efficiency are related as

$$\omega\varepsilon = D(E) \tag{1-36}$$

When measuring cylindrical sources, the efficiency, D(E), must be integrated over the source thickness, h', such that

$$I(E) = \frac{1}{h'_o} \int_o^{h'_o} D(E)dh' \tag{1-37}$$

where h'_o is the total source thickness. This integral has been numerically evaluated from the calculated values of D(E) and increments of h' for the 4 in. x 4 in. NaI(Tl) detector. The values of D(E) were interpolated so that E = 0.61 MeV, 1.46 MeV, and 2.62 MeV corresponded to the measured photopeaks of U^{238}, K^{40}, and Th^{232} respectively.

The calculations of I(E) were verified by measuring samples of potassium chloride containing K^{40} with an isotopic abundance of 1.18×10^{-4}. The measured concentration of potassium was found to deviate by less than about 5% from the actual concentration of 52.7%, using various sample thicknesses, as shown in Figure (1-10). Values of I(E) are given in Table (1-3) for the three photopeaks. The calculation of sample concentration is discussed in Section 5-3. The number of photons from the cylindrical source is then given by

$$N'_s = \frac{N_p}{I(E)P} \tag{1-38}$$

where the geometrical efficiency is defined as

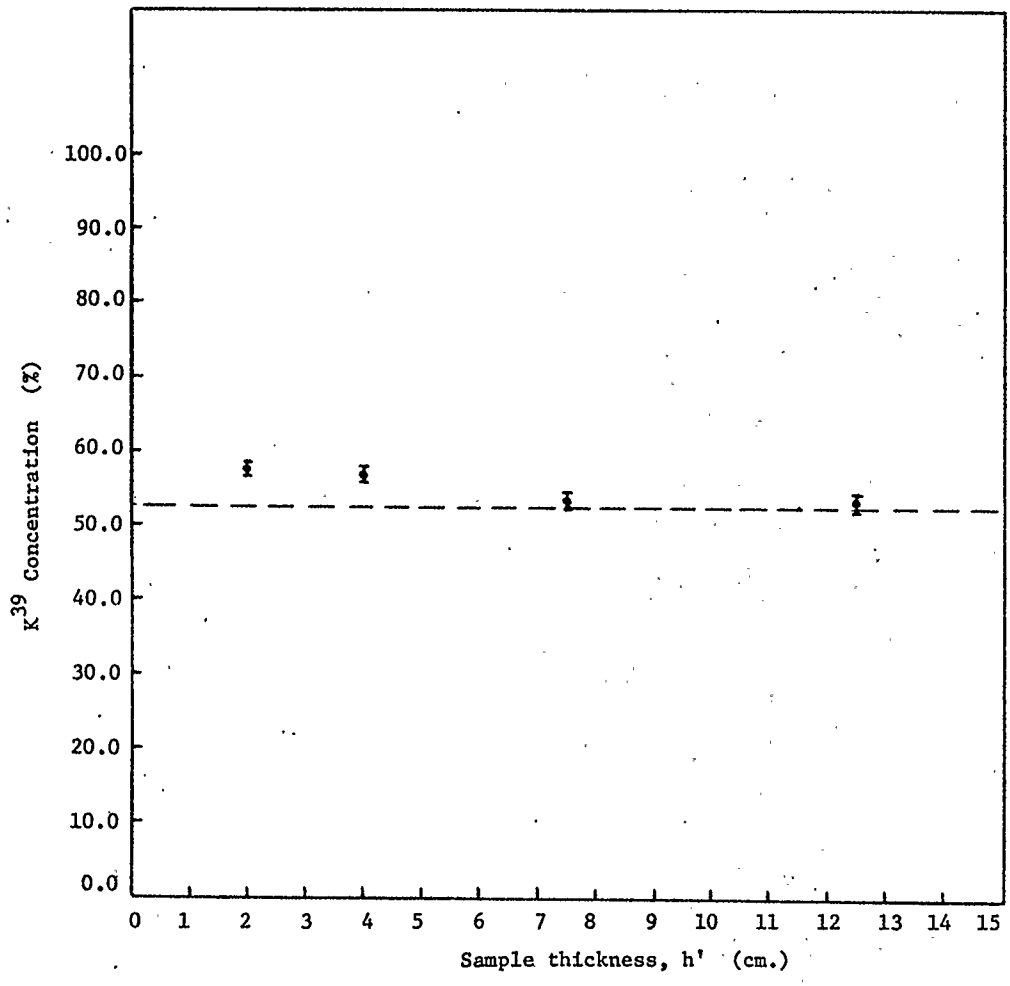

FIGURE (1-10) K^{39} concentration for samples of various thickness. (Dotted line represents the actual K^{39} concentration of KCl, 52.7%).

TABLE (1-3)

Detection Efficiencies, I(E)

r_o = 2 in., t_o = 4 in., R = 3/4 r.

h_o(cm) \ E(MeV)	0.61	1.46	2.62
2.0	0.24703	0.19961	0.17309
4.0	0.19064	0.15383	0.13353
7.5	0.14050	0.11343	0.09869
12.5	0.09808	0.07937	0.06924
17.5	0.07533	0.06108	0.05338
22.5	0.06113	0.04963	0.04343

$$M = [I(E)P]^{-1} \tag{1-39}$$

For I(E) of 0.14050, 0.11343, and 0.09869 and peak-to-total ratios of 0.66, 0.42, and 0.30 corresponding to the photopeaks at 0.61 MeV, 1.46 MeV, and 2.62 MeV respectively, the geometrical efficiencies for a sample thickness of 7.5 cm are 10.78, 20.99 and 33.77.

CHAPTER 2

BACKGROUND RADIATION AND SHIELDING

2.1 Introduction

When measuring gamma radiation from very dilute samples, it is essential that the background radiation observed by the NaI(Tl) detector be minimized. This background consists of natural environmental radiation from the earth's crust and atmosphere plus the portion of cosmic radiation which is able to penetrate the atmosphere and reach the earth's surface. This chapter describes the radiation contamination sources of background which originate from local environmental and instrumentational sources. Also discussed will be the primary cosmic radiation incident at the top of the atmosphere and the secondary cosmic radiation which is observed at ground level. Finally, the effect of shielding on reducing the components of the background radiation is presented.

2.2 Radioactive Contamination Sources of Background

In cases where radioactive contamination is a source of background, the problem may be contamination with either naturally occurring or man made radioisotopes. Although it is difficult to separate the background-contributing materials as to whether they are associated with the environment, instrument, shield, etc., such a separation can be made for the purpose of identifying these sources. Environmental contributors to the background originate in the atmosphere and at the earth's surface. Instrumental contamination can be caused by radioisotopic

sources in the crystal, crystal container, or photomultiplier tube. The shield itself may also contain radioactive sources.

Atmospheric sources including radon (Rn), thoron (Tn), and gaseous fission products contribute to the background spectrum. These sources are often troublesome as they are able to pervade the shield unless an inert atmosphere such as nitrogen is introduced into the detector region.

The airborne source of background is not constant with time, making it impossible to subtract a single background spectrum from the sample spectrum. Radon levels in air may vary by as much as a factor of 40 (May and Steingraber, 1958) and can result in fluctuations of up to 250 counts/min. in a whole-body counter inside a large-volume shield (May and Marinelli, 1961). The cyclic variations during a 24-hour period may show a radon content in air dropping below 10^{-13} curie/litre (1 curie = 3.7×10^{10} disintegration/sec) during the day and rising to 10^{-12} curie/litre at ground level during the increased stability of the early morning hours.

A tabulation (Lowder and Solon, 1956) has been made for air contaminants where radon gas from concrete may become concentrated in rooms in which there is little air motion. It has been found that, on the average, 4×10^{-12} curie/sec. of Rn and Tn are emitted by a cm^2 of the earth's surface. Concrete and other building materials may emit even more. Thus, it is estimated that there are 10^{-13} to 10^{-14} curies/litre of Rn and Tn in the air under normal conditions.

An expression has been calculated (Hultquist, 1956) for the ionization in air due to Rn and Tn as

$$I_{Rn} = 0.97 \times 10^{15} C_{Rn} \text{ ion pairs/litre sec.} \quad (2\text{-}1)$$

$$I_{Tn} = 0.96 \times 10^{15} C_{Tn} \text{ ion pairs/litre sec.} \quad (2\text{-}2)$$

where C is the content of the particular isotope in curies/litre. Common values of C_{Rn} and C_{Tn} are 5×10^{-14} curie/litre which give a value for I of 50 ion pairs/ litre sec. which is usually negligible compared to other sources of background.

The radioisotope concentrations can be converted into gamma ray flux at the detector using the relation (McCall, 1960)

$$n = \frac{q}{\mu_a/\rho} \quad (2\text{-}3)$$

Here, n is the effective number of gamma ray photons at the detector located in the centre of a spherical region (often the shield); the units are photons/cm^2 sec. The number of photons emitted per sec-gm. of shield material is denoted by q. The absorption coefficient of the shield material for the emitted gamma ray energy in cm^2/gm is given by μ_a/ρ. If n is the total flux of photons of all energies, the expression gives a lower limit for the number penetrating the medium because it essentially accounts for only the attenuated primary gamma photons passing through the shield or space surrounding the detector and does not include the buildup of scattered photons which have been degraded in energy. However, if the background spectrum contains monoenergetic lines which identify particular radioisotopic contaminants and if only the counts in the monoenergetic peak are used to determine n, Equation (2-3) will give a correct

evaluation of q. For example, if it is assumed that all of the counts in the 2.62 MeV photopeak of the background spectrum of Figure (4-6) originate from the Th^{232} contaminant within the iron shielding, then the 8 counts/min. activity of this element is 5×10^{-16} curie/gm. The absorption coefficient for iron is found in Figure (2-1).

Application of Equation (2-3) to Rn or Tn concentrations in the air surrounding the NaI(Tl) detector gives an estimate of the background radiation produced by these sources. A value of q = 4×10^{-12} curie/liter can be converted into 1.5×10^{-4} photons per second per cm^3 of air. From Figure (2-2) the absorption coefficient for air at 1 MeV is 6.5×10^{-2} cm^2/gm. Using the density of air as 1.3×10^{-3} gm/cm^3, one obtains a value for n of 2 photons/cm^2 sec. Over the surface area of a 4 in. x 4 in. crystal this becomes 5×10^4 photons/min. The mean free path of 1 MeV photons in air for which this flux occurs is 120 m. The integrated background rate from 0.1 to 3 MeV for the 4 in. x 4 in. crystal in the laboratory was found to be about 2×10^4 counts/min.

Radioactive sources in the earth also contribute to the background spectrum. Expressions for ionization above the earth's surface (approximately independent of height up to one mean free path in air) due to several sources have been given (Hultquist, 1956):

$$I_{Ra} = 1.26 \times 10^{12} S_{Ra} \qquad (2\text{-}4)$$

$$I_U = 0.44 \times 10^6 S_U \qquad (2\text{-}5)$$

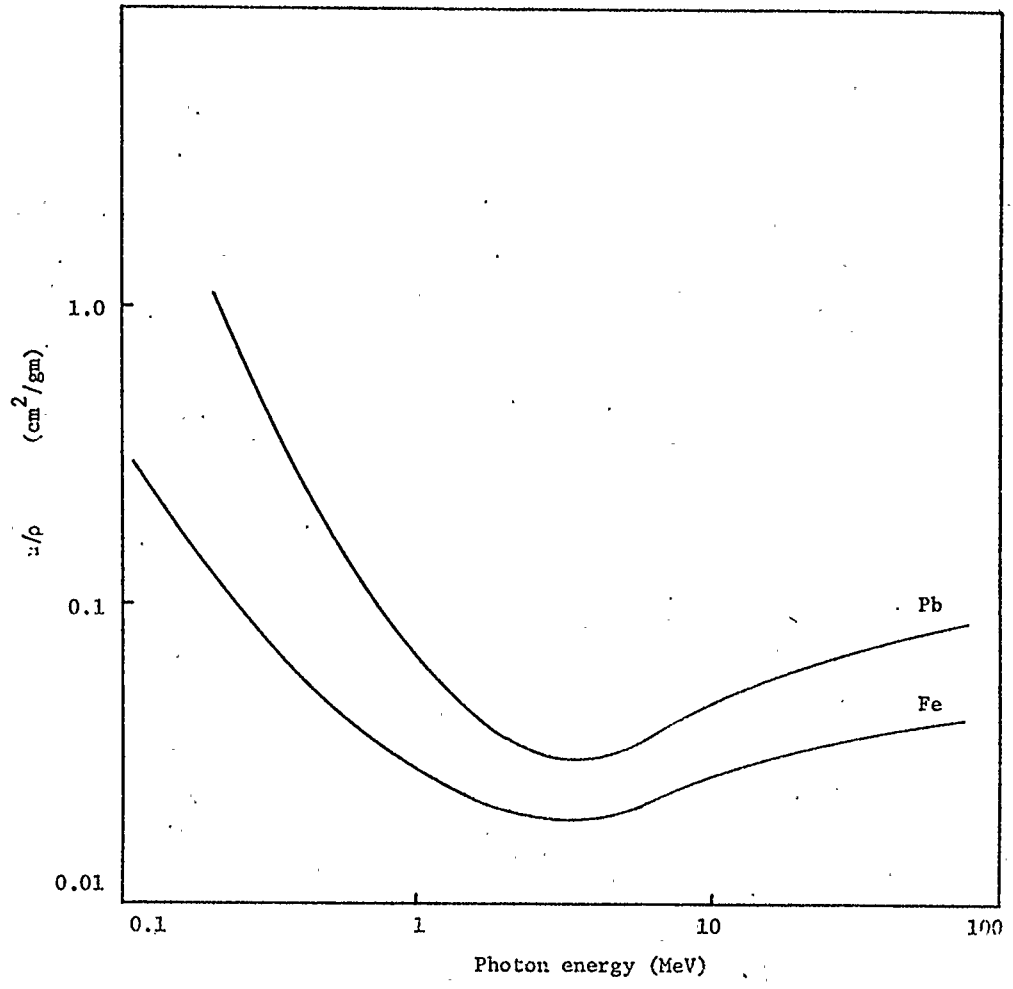

FIGURE (2-1) Mass absorption coefficients for high-Z materials. (From Rockwell, 1956).

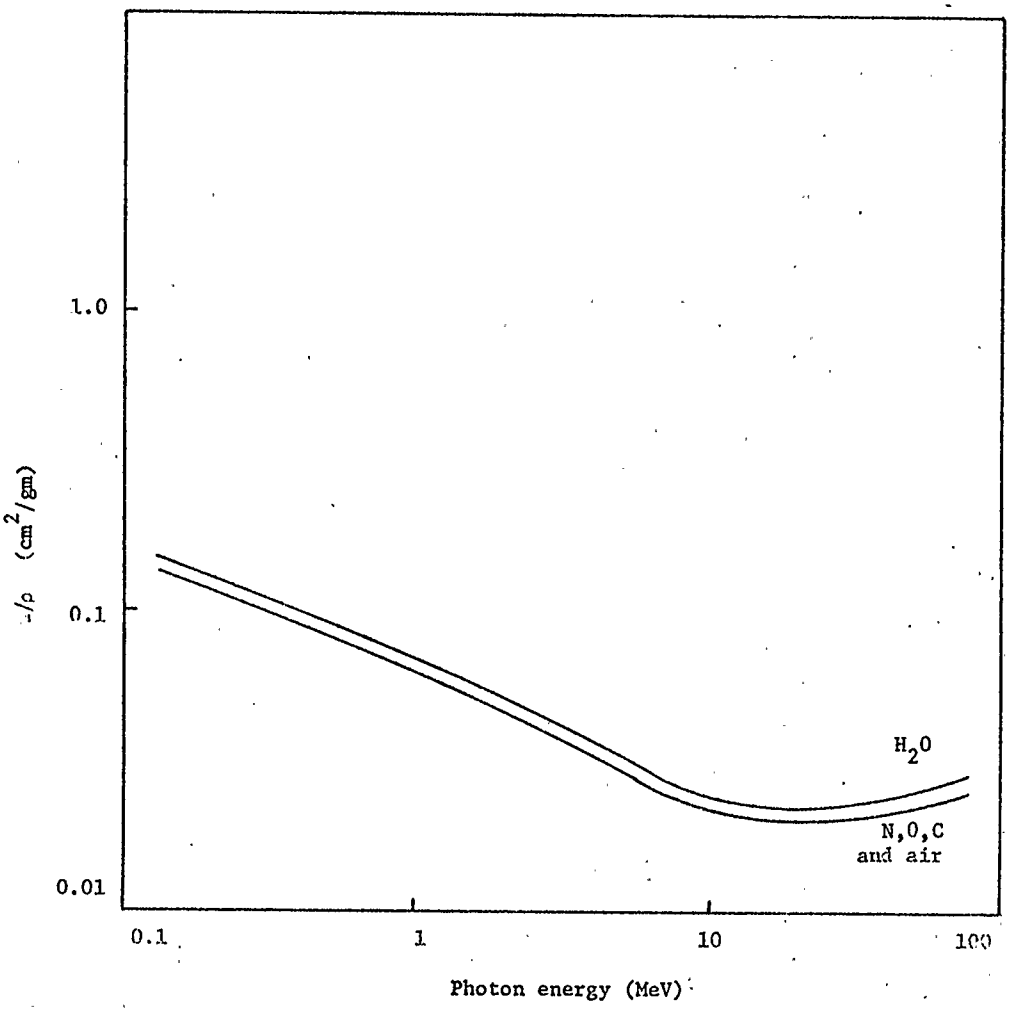

FIGURE (2-2) Mass absorption coefficients for low-Z materials. (From Rockwell, 1956).

$$I_{Th} = 0.21 \times 10^{6} S_{Th} \qquad (2\text{-}6)$$

$$I_{K} = 91 \times S_{K}39 \qquad (2\text{-}7)$$

where I is the ionization in ion pairs/litre sec in air and S is the isotope content of the mineral in gm. of isotope per gram of mineral. Typical isotope contents of various rocks are given in Table (2.1). It can be seen that these values of S, when substituted into the above formulae, lead to much higher ionization rates than for the gaseous materials. Substituting the largest value (120 gm Ra/gm x 10^{12}) into Equation (2-3) gives a photon flux of 140 photons/cm^2 sec. at the centre of a rock shield.

Instrumental components of the spectrometer including the NaI(Tl) crystal, crystal container, and photomultiplier tube may contribute to the background. The NaI(Tl) crystal contains natural potassium which, in general, emits 27 beta particles/gm sec. due to the K^{40} isotope (Sharpe, 1955). Analyses of early type crystals (De Voe, 1961) indicated K^{40} contents as high as 55 ppm, but more recent efforts by manufacturers have reduced this to about 1 ppm. It has been shown (Marinelli et al., 1961) that a 20 cm x 10 cm crystal containing 1 ppm K^{40} will produce 20 beta disintegrations per minute. When the absolute intensity for K^{40}, A = 0.11, is considered (see Section 5-3) this results in two 1.46 MeV photons per minute. The volume of the above crystal is four times that of the 4 in. x 4 in. crystal used in this experiment so that 0.5 counts per minute would be expected at 1.46 MeV. The measured background in this photopeak was found to be 20 cpm which indicates

TABLE (2-1)

Natural radioisotope concentrations in various rocks

(From Shafroth, 1967)

Mineral	S		
	g $Ra^{226}/gx10^{12}$	g $Th^{232}/gx10^{6}$	g $K^{39}/gx10^{2}$
Igneous Rocks:			
Average:	1.3	12	2.6
Granites:			2.9-3.55
North America	1.6	8.1	
Finland	4.7	28	
Alps	4.4	33	
Basalts:			1.3
North America	0.96	9.8	
England, Germany, etc.	1.3	8.8	
Sedimentary Rocks:			
Sandstone	0.3	5	1
Limestone	up to 1.5	1	0.1-0.5
Alum. Shalesin, Sweden	up to 120	0.6-2	3.5

that additional sources of K^{40} are contributing.

The NaI(Tl) crystal is partially surrounded by Al_2O_3 and hermetically sealed in an aluminum container with a glass window at one end. Aluminum has been found to contain up to 3×10^{-13} curie of Ra per gm. of Al. The glass used in the crystal window will usually contain K^{40} and is thought to be a major source of the 1.46 MeV background peak. Another source of K^{40} is the glass in the photomultiplier tube.

2.3 Cosmic Radiation Sources of Background

The chemical composition of the primary cosmic radiation has been summarized in Table (2-2) (Ginzburg, 1969). To increase the statistical accuracy, data have been obtained for groups of nuclei rather than for individual particles. The nuclei of lithium, beryllium, and boron where Z = 3, 4, 5 respectively constitute the group of light nuclei (L groups). The nuclei of carbon, nitrogen, oxygen, and fluorine in which Z = ¢, 7, 8, 9 form the group of medium nuclei (M group). Nuclei with $10 \leq Z < 20$ are classified as heavy nuclei (H group), and nuclei with $Z \geq 20$ are classified as very heavy nuclei (VH group). Protons (p group) and helium nuclei or α-particles (α group) are considered separately.

The intensity, I, is the number of particles incident upon a unit area per unit time per unit solid angle; in this case, I is measured in particles/m^2 ster. sec. The flux is obtained by integrating I over the solid angle. For isotropic radiation with integration over a hemisphere,

$$F = \int I \cos\theta \, d\Omega = \pi I \qquad (2\text{-}8)$$

TABLE (2-2)

Chemical composition of primary cosmic rays

(From Ginzburg, 1969)

Nuclear group	Z	$\overline{A}$	I	$\overline{AI}$	$\frac{I}{I_H} = \frac{N}{N_H}$	Inter-stellar gas N/N_H
p	1	1	1300	1300	650	3360
α	2	4	94	376	47	258
L	3-5	10	2.0	20	1.0	10^{-5}
M	6-9	14	6.7	94	3.3	2.6
H	$\geq$10	31	2.0	62	1.0	1.0
VH	$\geq$20	51	0.5	25	0.3	0.06

The intensities for the various nuclei groups are listed in Table (2-1). $\bar{A}$ is the average atomic weight for each group, and $\bar{A}I$ indicates the number of nucleons in the cosmic-ray flux. This data refers to particles with total energies greater than 2.5 GeV/nucleon.

The sixth column of Table (2-2) shows the ratio of the nuclei flux in a given group to the flux of nucli in group H; this ratio is also equal to the ratio N/N_H of the concentrations of nuclei in the corresponding groups. Here, for an isotropic angular distribution of particles, the concentration is

$$N = 4\pi I/v \qquad (2\text{-}9)$$

where v is the particle velocity; for the relativistic particles considered, $v = c = 3 \times 10^{10}$ cm/sec. In the last column of Table (2-2) are presented ratios N/N_H characterizing the average abundances of the elements in the sun, stars, and interstellar medium.

The chemical composition of primary cosmic rays has two important characteristics. First, only a very small amount of the light elements (lithium, beryllium and boron) exists in stellar and interstellar regions since these elements are rapidly burned in stellar interiors. In local primary cosmic rays, however, the elements of the L group are about as abundant as the heavy elements, that is, they are about 10^5 times more abundant than in the Galaxy. The presence of the L group in the primary cosmic rays can be explained as follows. As cosmic rays move through interstellar space, the nuclei of groups M and H become divided as a result of nuclear collisions with the nuclei of atoms of the interstellar medium

(mostly protons and helium nuclei). Some of these disintegration products are nuclei of the L group.

Second, primary cosmic rays are relatively richer in heavy and very heavy elements when compared with celestial objects. In cosmic rays, there are approximately 700 protons and α-particles for every nucleus of the H group and about 2000 protons and α-particles for every nucleus of the VH group. In contrast, the value for the Galaxy is about 3600 protons and α-particles per nucleus of group H and 60000 protons and α-particles per nucleus of group VH. Thus, cosmic rays have five times as many heavy elements and thirty times as many very heavy elements as the stars and interstellar gas.

Secondary cosmic radiation which penetrates the earth's atmosphere is conventionally classified as having a hard and soft component where, in the former case, radiation penetrates 10 cm. of lead, and in the latter case this thickness of lead is sufficient to absorb the radiation (Rossi, 1952). It is convenient, when discussing shielding materials, to group the secondary cosmic rays into hard, nucleon, and soft components in which typical particles of the groups are muons, neutrons, and electrons respectively (Shafroth, 1967).

All of these components at sea level are secondary radiations from interactions which the primary cosmic rays initiate in the upper atmosphere at altitudes of about 15 km. The primary cosmic rays are sorted by the earth's magnetic field and are influenced by solar events; the secondary flux, however, is influenced little by these effects. At sea level, the flux of secondary particles is primarily downward with an angular distribution varying approximately as $\cos^n\theta$, where θ is the zenith angle and n is a function of particle

type and energy. The components of the secondary cosmic radiation in the earth's atmosphere are illustrated in Figure (2-3).

The hard component of cosmic rays at sea level consists of muons having a rest mass of 105.6 MeV and a half-life at rest of 2.2×10^{-6} sec. These particles occur in both charge states, and as a result of the positively charged primary cosmic rays, those with positive charge are about 25 per cent more abundant. The vertical intensity, I_v, under 167 gm/cm^2 of lead is 8.2×10^{-3} muons/cm^2 ster sec. (Rossi, 1948) as measured at 40°N latitude and remains essentially constant north of this latitude.

The muon and nucleon energy spectra (Pine, Davisson and Greisen, 1959) are shown in Figure (2-4). The measurements of muons and protons were made with magnetic spectrographs detecting vertically incident particles only in which the intensity is known to vary with zenith angle, θ, as $\cos^n\theta$; the value of n is energy dependent. For muons, a constant value of n = 2 is sufficiently accurate, whereas the value of n for protons is in the range of 5-7. In order that the muon and proton spectra be comparable with the neutron spectrum, which was obtained with direction-sensitive detectors, the omni-directional flux of muons and protons has been calculated from the relation

$$F(E) = \int I_v(E) \cos^n\theta d\Omega$$

$$= \frac{2\pi}{n+1} I_v(E) \qquad (2\text{-}10)$$

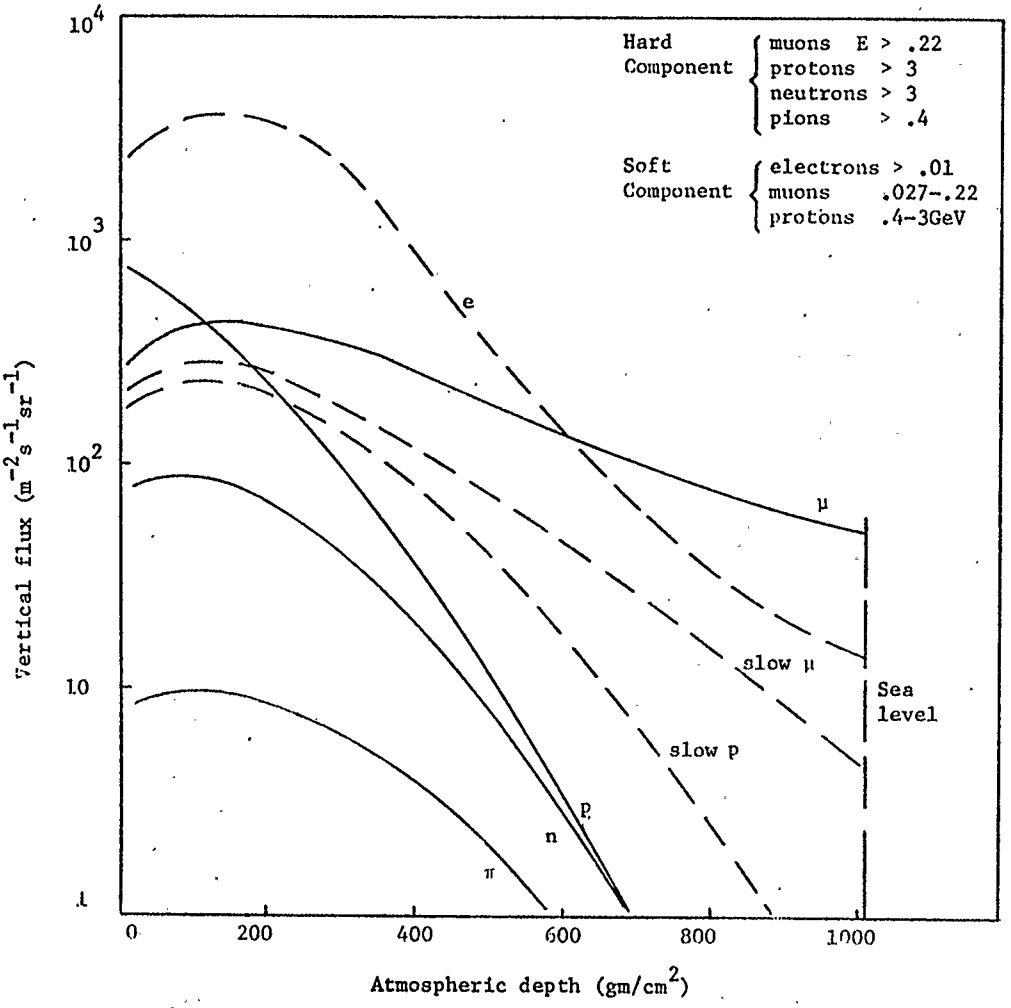

FIGURE (2-3) Components of the cosmic radiation in the atmosphere. (From Hillas, 1972).

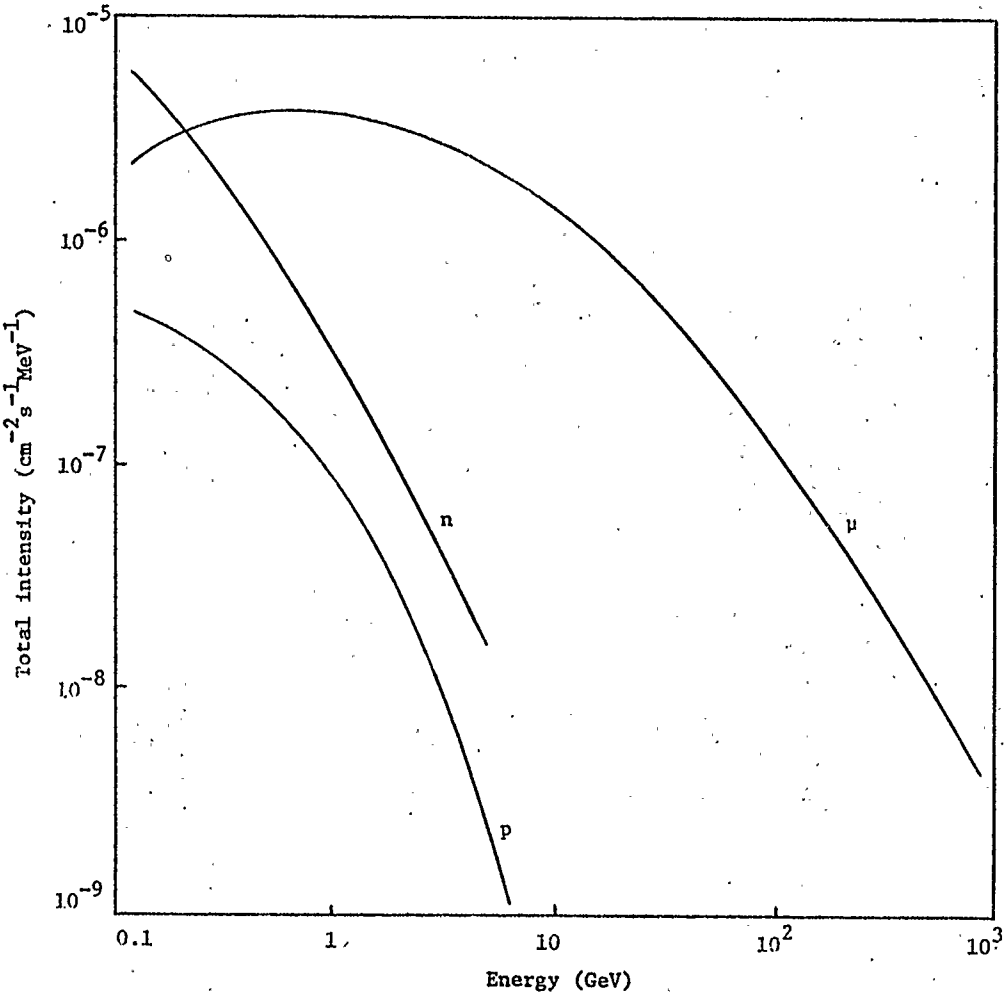

FIGURE (2-4) Omnidirectional differential energy spectrum of muons and nucleons near sea level. (From Pine, Davisson, and Greisen, 1959).

For n=2, the muon flux is 1.7×10^{-2} particles/cm^2 sec. O'Brien (1972) gives the value of muon flux at an atmospheric depth of 1033 gm/cm^2 (sea level) as 1.90×10^{-2} particles/cm^2 sec.

Cosmic-ray muons lose their energy primarily through the processes of ionization and collision since radiation, pair production and Cerenkov losses contribute only at incident energies above 40 GeV. The process of muon interaction with the NaI(Tl) detector is discussed next, while this interaction with the iron shield is described in Section 2.4.

The probable energy loss of a single charged particle in a thickness, t cm, of material is given by (Landau, 1944)

$$\varepsilon_{prob} = \frac{2\pi ne^2 t}{mv^2}\left[\ell n\left(\frac{2mv^2(2\pi ne^4 t/mv^2)}{I^2(1-\beta^2)}\right) - \beta^2 + j - \delta\right] \qquad (2\text{-}11)$$

where n is the electron density, e is the electronic charge, m is the mass of the electron, I is the average ionization potential of the material, and v is the velocity of the charged particle. The term j is a small correction factor calculated from straggling theory which depends on the absorber thickness and the particle velocity and which approaches 0.37 when

$$\frac{2\pi ne^4 t}{mv^2} << \frac{2mv^2}{1-\beta^2} \quad . \qquad (2\text{-}12)$$

The term δ represents a density effect correction which arises because the polarization of the medium reduces the energy loss. Numerical values of δ have been calculated (Steinheimer, 1953) for sodium iodide. Steinheimer also calculated the mean ionization

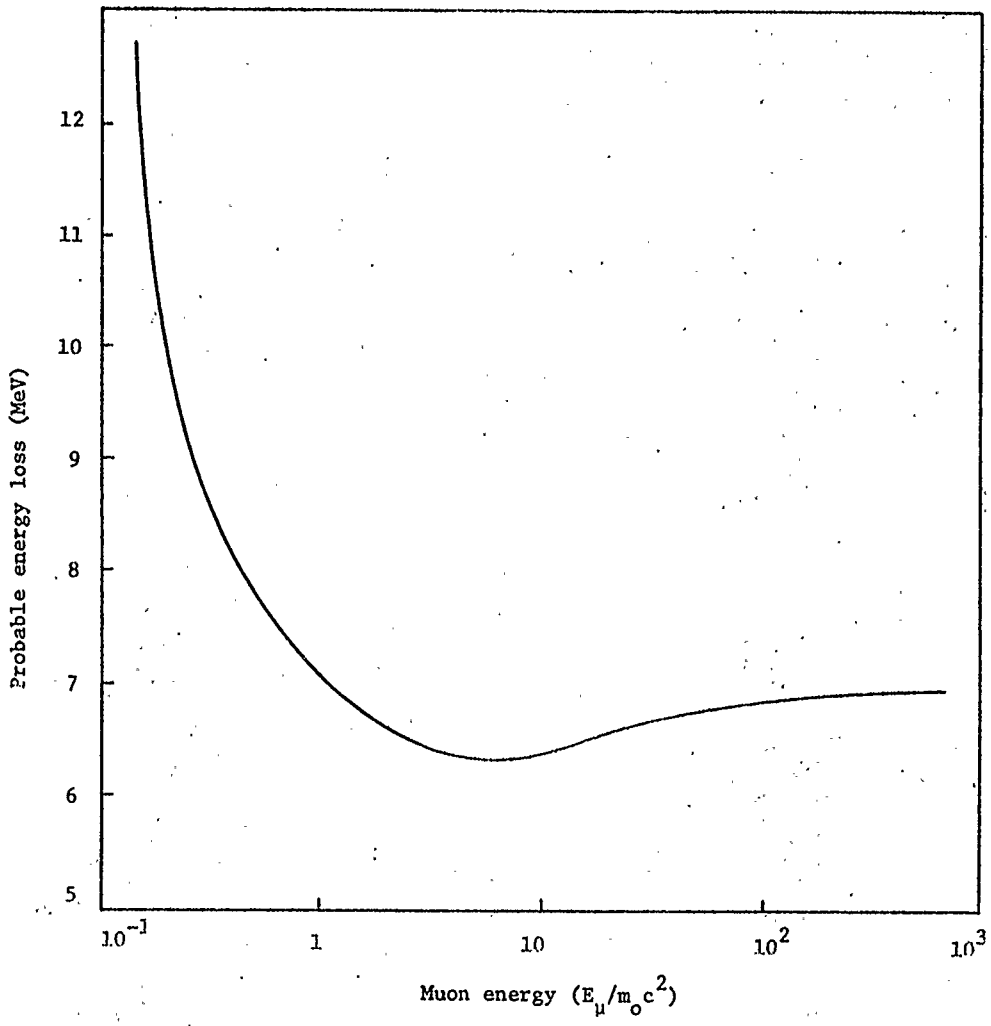

FIGURE (2-5) Probable energy loss of muons in 1.51 cm. of NaI(Tl). (From Bowen, 1954).

potential for sodium iodide according to the relation

$$I_{av}^{2} = I_{Na}^{2(0.172)} \; I_{I}^{2(0.828)} \qquad (2\text{-}13)$$

which gives I = 392eV where 0.172 and 0.828 are the electronic compositions of Na and I respectively.

Equation (2-11), as a function of meson energy, is shown in Figure (2-5) for a 1.51 cm sodium iodide crystal. From Figure (2-4) it is evident that the average energy of cosmic ray muons is approximately 1 GeV which corresponds to a probable energy loss of 7 MeV in 1.5 cm or about 5 MeV/cm of NaI. For a 4 in. x 4 in. crystal, a muon will lose 50 MeV.

The omnidirectional integral energy spectrum of the soft (electromagnetic) component of secondary cosmic rays is shown in Figure (2-6). Above 100 MeV, the ordinate is the total number of electrons and photons, assumed to be approximately equal in number. In the lower-energy region the dotted line represents the electron flux only; the flux of electrons with energies greater than about 1 MeV is 8.4×10^{-3} particles per unit sphere per sec.

2.4 Shielding

The three components of the ground level cosmic radiation have been described in Section 2.3. The muon component, the nucleon component, and the soft component produce different contributions to the background spectra, depending upon the energy region considered, and the shielding requirements to reduce these contributions are somewhat different for each. From Section 2.2 it is evident that ordinary rock shields while reducing environmental contaminants will

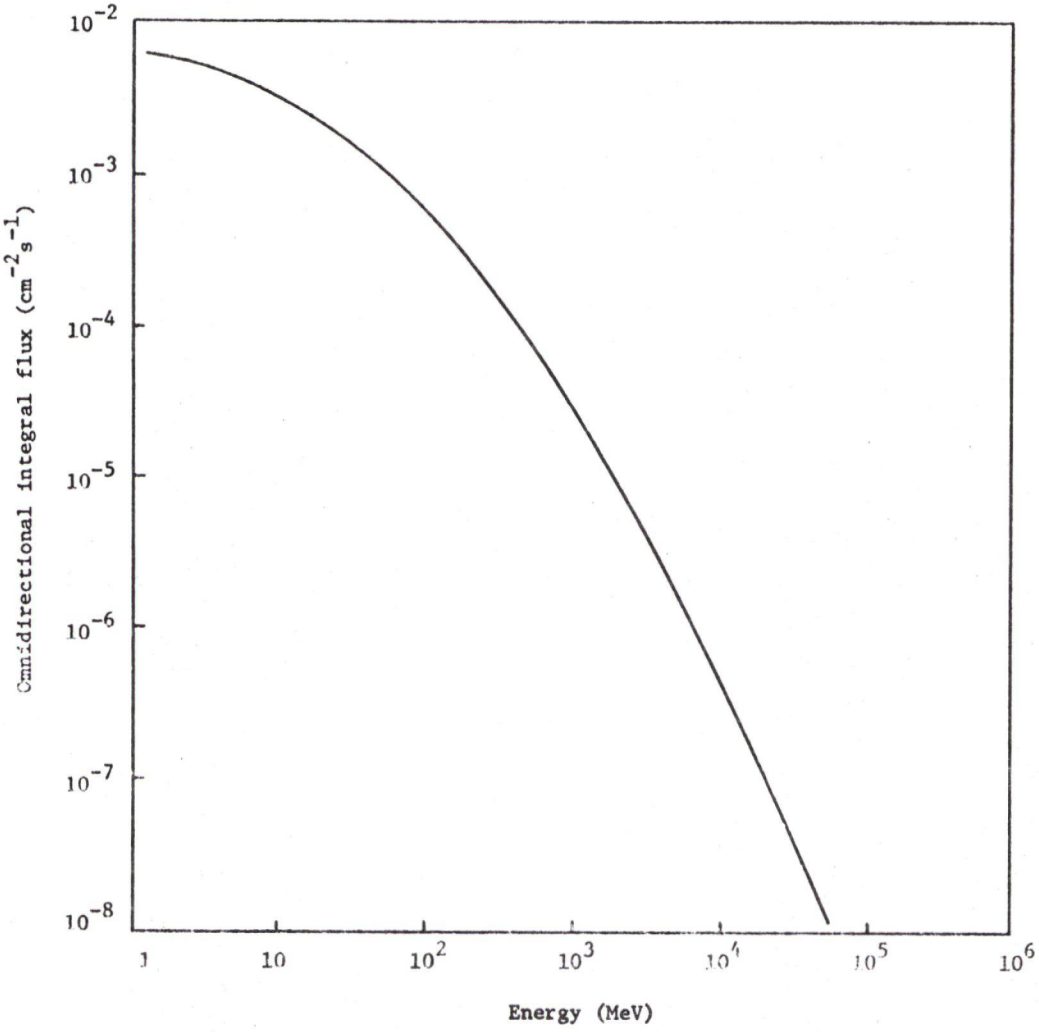

FIGURE (2-6) Omnidirectional integral energy spectrum of electrons and photons near sea level. (From Carmichael, 1957).

also generate a large photon flux. Thus, shields are usually chosen from materials such as lead or iron, the former being substantially more expensive.

Used in this experiment was a cylindrically shaped iron shield, 120 cm. in height, with an inside diameter of 20 cm. and outside diameter of 44 cm.; the wall thickness and removable top thickness are 12 cm. The lower 60 cm. has been constructed from pre-World War II iron to ensure that no Co^{60} is present. The upper 60 cm. was formed from cast iron; gamma ray spectrometry of a sample of this material verified the absence of Co^{60} in this segment.

Shielding requirements to reduce the muon flux present the greatest difficulty since these particles are the most penetrating and because they have the highest intensity of all secondary cosmic rays at ground level. Forty meters of water or its equivalent gives a ten-fold reduction of the muon intensity; for the next order-of-magnitude reduction, an additional 120 m of water is required. Figure (2-7) shows the distance travelled by muons of different initial energies in various materials (Grinberg and Le Gallic, 1961).

Assuming an average shielding path length of 50 cm., the range-energy relation for muons indicates that muons of energy less than 0.60 GeV will lose all of their energy in the iron shielding. From the muon energy spectrom of Figure (2-4) it can then be calculated that approximately 15% of the incident muons will lose all of their energy in the shield. The total surface area of the shield is 1.2×10^4 cm^2 and the omnidirectional muon flux is 1.9×10^{-2}

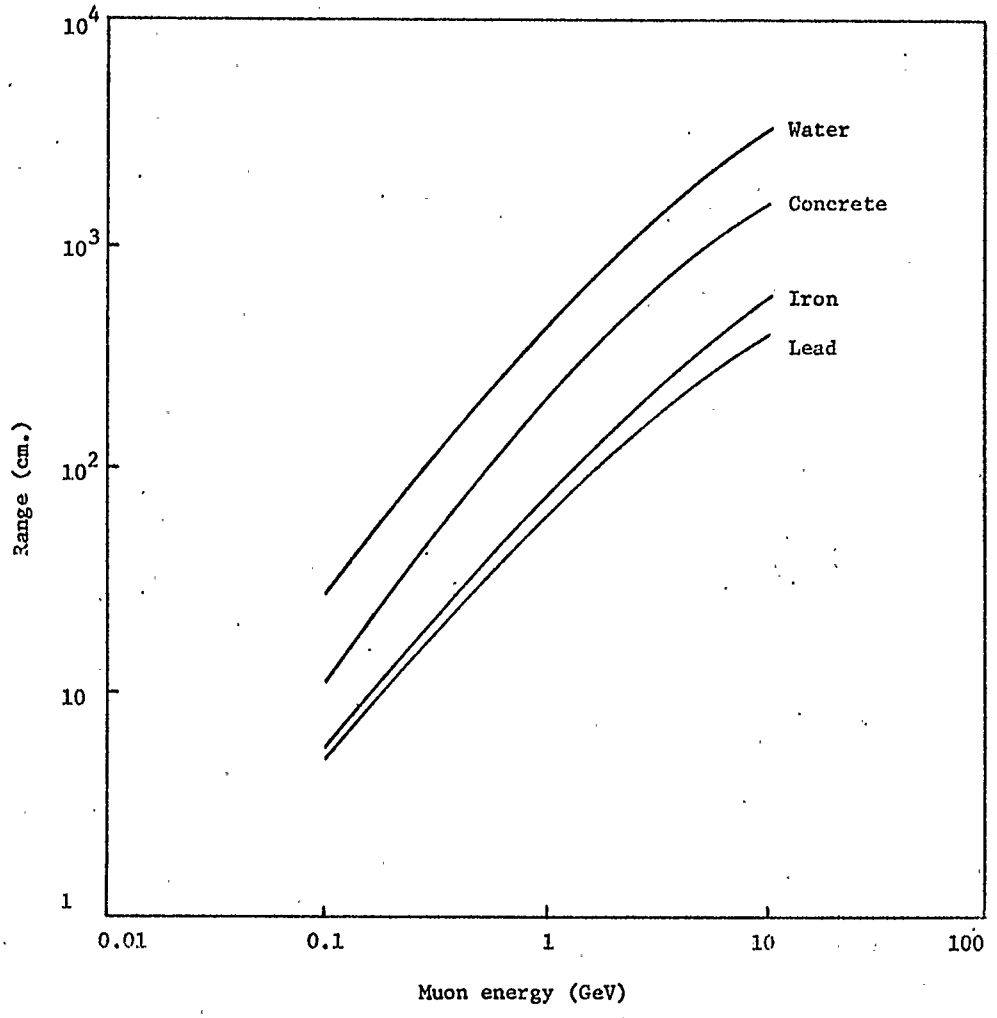

FIGURE (2-7) Range-energy relation for muons. (From Grinberg and Le Gallic, 1961).

particles/cm^2 sec so that 2×10^3 muons/minute will come to rest in the shield.

When muons come to rest in condensed material, they may decay, or negative muons may be captured by the nucleus. The decay reaction is given by

$$\mu^{\pm} \rightarrow e^{\pm} + 2\nu, \qquad (\nu = \text{neutrino}) \tag{2-14}$$

The probability of μ^- capture increases with the atomic number of the interacting medium and is equal to the decay probability at Z = 11. The electron energy spectrum from muon decay in liquid hydrogen (Plano, 1960) has shown that the most probable and maximum energies are 46 and 53 MeV respectively. This implies that decay electrons in shielding materials are of sufficient energies to generate electron-photon showers, and, hence contribute to the low-energy photon flux which can reach the NaI(Tl) detector and contribute to the background spectrum.

Negative muons can be captured according to the relation

$$\mu^- + {}^{A}_{Z}X \rightarrow {}^{A}_{Z-1}X \rightarrow n + {}^{A-1}_{Z-1}X + \nu \tag{2-15}$$

This process releases about 100 MeV, of which the largest fraction is carried away by the neutrino. The remainder may be carried off by a single neutron, but in heavy nuclei it is usually shared by the entire nucleus. The "nuclear temperature" is increased with a subsequent release of one or more neutrons. These "evaporation" neutrons have most probable energies of only a few MeV. Several gamma rays with energies in the range of 1-10 MeV are emitted to

complete the de-excitation of the residual nucleus.

High-energy nucleons, although numerically less abundant than muons, also contribute significantly to the low-energy gamma-ray background. Integration of the omnidirectional differential energy spectrum, Figure (2-4) gives the total incident particle flux. In the energy range of 100 MeV to 100 GeV, a flux of 1.6 x $10^{-3}/cm^2$ sec. for neutrons and 2.2 x $10^{-4}/cm^2$ sec. for protons is found.

The processes by which high-energy nucleons interact in dense materials are similar in principle to the reactions in air which produce the nucleonic component of cosmic rays but differ in detail because of the higher atomic number. These reactions are pion production, spallation, direct nuclear cascade, and emission of low-energy evaporation particles which accompany de-excitation of the residual nucleus (Jackson, 1956). The number of evaporation neutrons produced by nucleonic cascades varies roughly with atomic mass number as $A^{2/3}$. The average number of evaporation neutrons per interaction has been found to be 2.9 in iron and 6.5 in lead (Bertini and Dresner, 1962) with an average energy of 10 MeV. The collision mean-free-path of the nucleonic component for several materials is given in Table (2-3).

The number of photons resulting from neutron inelastic scattering and from capture in the resonance and thermal energy regions may be calculated in principle from the transport and moderation properties and interaction cross-sections of the shielding material. The calculations are straightforward for an

TABLE (2-3)

Collision mean free path of the nucleonic component in various materials

(From Shafroth, 1967)

Absorber	Mean free path (gm/cm^2)
Air	120
Concrete	145
Carbon	166
Aluminum	200
Lead	300

infinite-slab geometry; however, neutron leakage at the shield surfaces is important for practical configurations, and the transport equations can be solved only approximately. The thermal capture gamma-ray spectra are well known for most elements of interest. Principal photons from thermal capture range in energy from 2.23 MeV in hydrogen to 7.40 and 7.64 MeV in lead and iron respectively. Photon spectra resulting from the capture of thermal neutrons in various shielding materials is illustrated in Figure (2-8).

Attenuation of the soft component electrons and photons occurs primarily by radiation and pair production in the field of the absorber nuclei. If it is assumed that these are the only processes which occur during attenuation, the build-up and decay of a cascade shower in a think medium may be calculated (Rossi, 1952). However, in the shielding context since the photon energy range of interest (0.1 to 3 MeV) is that in which Compton scattering and photoelectric absorption must also be considered, shower theory cannot give meaningful estimates of the required shielding thickness. A computational method which includes all significant energy losses and cross-sections, thus giving accurate results down to about 5 MeV, has been described (Olson and Spencer, 1958). The Monte Carlo method has been used to simulate the statistical fluctuations of shower generation in lead (Wilson, 1952), but results for iron in the energy range of 0.1 to 3 MeV are not available. Transition curves (Rossi, 1952) indicate that 10 cm. of lead (equivalent to 17 radiation lengths or to 30 cm. of iron) are required to suppress the shower electrons, whereas photons of a few MeV (in the broad minimum of the absorption coefficient characteristic of high Z materials) penetrate even deeper.

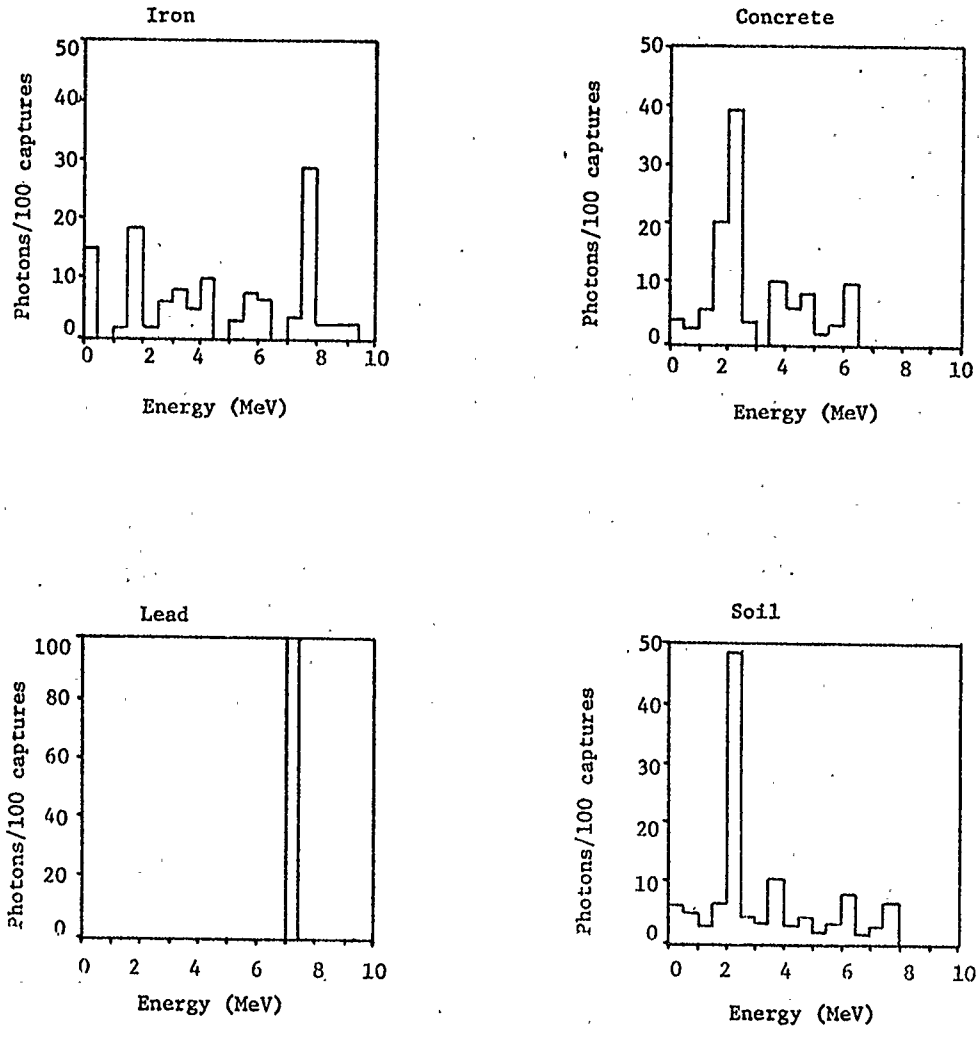

FIGURE (2-8) Energy spectra of photons emitted after capture of thermal neutrons in various shielding materials. (After Adams and Gasparini, 1970).

It has been estimated (Shafroth, 1967) that only approximately 1 per cent of the incident electron-photon shower energy is emergent from 20 cm. of iron (11 radiation lengths). Thus, for the 12 cm. shield used in this experiment, about 2 per cent of the shower will penetrate, and the soft component of cosmic radiation will not contribute significantly to the 0.1 to 3 MeV background spectrum.

The integrated background counting rate of the NaI(Tl) detector inside the shield in the 0.1 to 3 MeV region was found to be 1204 ± 4 counts/min. It now becomes necessary to determine whether this background flux can be reduced by a liquid scintillation connected in anticoincidence with the NaI(Tl) crystal.

CHAPTER 3

LIQUID SCINTILLATOR

3.1 Introduction

Although the iron shielding is effective in reducing the environmental and soft cosmic ray contributions to the background spectrum, it will act as a source of low energy photons, neutrons, and charged particles which are produced by interactions of cosmic ray muons and nucleons with the shield (Adams and Gasparini, 1970). When it is desirable to reduce this background, a cost-effective choice must be made from among the various means of producing background reduction. A decrease of 98.8% of the muonic background has been observed when a proportional counter at sea level under shielding of 320 gm/cm^2 of concrete and lead was moved to a cave under 60 m of calcareous rock, corresponding to a shielding of 15,000 gm/cm^2 (Delibrias and Repaire, 1967). Another approach is to surround the NaI(Tl) detector with an anticoincidence NaI(Tl) annulus. The expense of using a sodium iodide annulus or extensive underground shielding can be reduced by employing either a plastic or liquid scintillator. The pulse height and resolution of these scintillators are comparable as are their cost (Birks, 1964). With a knowledge of the scintillation process, the efficiency of the scintillator can be determined. Then, the effectiveness of the scintillator in reducing the background can be evaluated.

3.2 Mechanism of Liquid Scintillation

The general scintillation mechanism has been discussed

qualitatively in Section 1.3. An organic (e.g., liquid) scintillator is analogous to an inorganic scintillator such as NaI(Tl) in the sense that the organic solvent corresponds to the crystal lattice, NaI, while the solute corresponds to the impurity atoms, Tl. However, because of its low density ($\sim$ 1 gm/cm^3) and the low atomic number of its constituent elements (H = 1, C = 6, N = 7, O = 8) an organic scintillator has much lower gamma ray absorption coefficients than an inorganic scintillator. Because of the low Z, photoelectric absorption is small when the gamma ray energy is E > 0.030 MeV, and Compton scattering is the primary gamma ray absorption process up to E $\sim$ 20 MeV, where pair production becomes appreciable. The Compton edge corresponding to electrons of energy

$$T_m = \frac{h\nu}{1 + \frac{1}{2}\frac{m_o c^2}{h\nu}} \qquad (3\text{-}1)$$

is the only significant peak which normally appears in the scintillation pulse-height spectrum. This edge corresponds to the high-energy end of the Compton distribution which has a finite width and which is further broadened by the finite resolution of the scintillation counter. The width of the Compton edge is therefore usually greater than that of the photopeak which occurs in scintillation pulse-height spectra from NaI(Tl) and which corresponds to the full gamma ray energy, $h\nu$. Consequently, the organic scintillators do not compare favourably with NaI(Tl) for gamma ray spectrometry.

However, organic scintillators possess two advantages over inorganic scintillators. A fast scintillation decay time

($\sim$ 2 ns) is important for fast coincidence detection of gamma rays, and large volumes enable high gamma-ray detection efficiencies to be attained. Calculation and measurement of this efficiency will be discussed in Section 3.4.

3.3 Description of the Liquid Scintillator

When a large volume of scintillator is required, or when the expense of large plastic or crystal scintillators would be prohibitive, liquid scintillators are well suited. The scintillator used in this experiment is mineral oil based produced by New England Nuclear; the scintillator formulation is proprietary. The outside diameter is 19 cm. with a wall thickness of 3 cm. and a height of 42 cm. The physical characteristics of the scintillator are given in Table (3-1).

3.4 Efficiency of the Liquid Scintillator

For detection by the liquid scintillator, a certain minimum photon energy must be transferred to a Compton electron. The cross section can be calculated (Roulston and Naqvi, 1957) by integrating the differential Compton cross section from the corresponding minimum photon scattering angle to 180°. The photon detection efficiency is then given by

$$\eta = 1 - e^{-\mu x} \qquad (3\text{-}2)$$

where $\mu = \rho_e \sigma$; ρ_e is the electron density which is 0.29×10^{24} electrons/cm^3, and σ is detection cross section in barns/electron. The quantity x is the scintillator thickness in cm. and has the

TABLE (3-1)

LIQUID SCINTILLATOR CHARACTERISTICS

(Nuclear Enterprises Scintillator Catalogue, 1973)

Property	Typical Values
Pulse height	30% of Anthracene
Mean free path (4000-5000Å)	Greater than 5 meters
Decay time	2.0 nsec
Refractive index at 25°C	1.485 ± 0.005
Peak fluorescence wavelength	4230Å
Flashpoint	175°F
Specific gravity at 25 C	0.89
Hydrogen:Carbon mole ratio	1.75:1.00 ± 0.05
Electron density	0.29×10^{24} electrons/cm^3

value of 3 cm. The dependence of η on incident photon energy is shown in Figure (3-1) for the liquid scintillator in the 0.1 to 3 MeV region.

Also shown in Figure (3-1) is the reduction in the photopeak intensity of several calibration sources as produced by the liquid scintillator. These photopeaks were recorded by the NaI(Tl) detector with the sources placed outside of the liquid scintillator. The intensities resulting when the liquid scintillator was turned off and on, I_1 and I_2 respectively, were measured and the reduction in the photopeaks of various photon energies is given by

$$d = \frac{I_1 - I_2}{I_1} \quad . \tag{3-3}$$

It can be seen that there is reasonable agreement between the theoretical photon detection efficiency of Equation (3-2) and the measured reduction in photopeak intensity of Equation (3-3). Equation (3-2) indicates that in order to attain a detection efficiency of 99% for 0.15 MeV photons, a liquid scintillator thickness of 22 cm. is required.

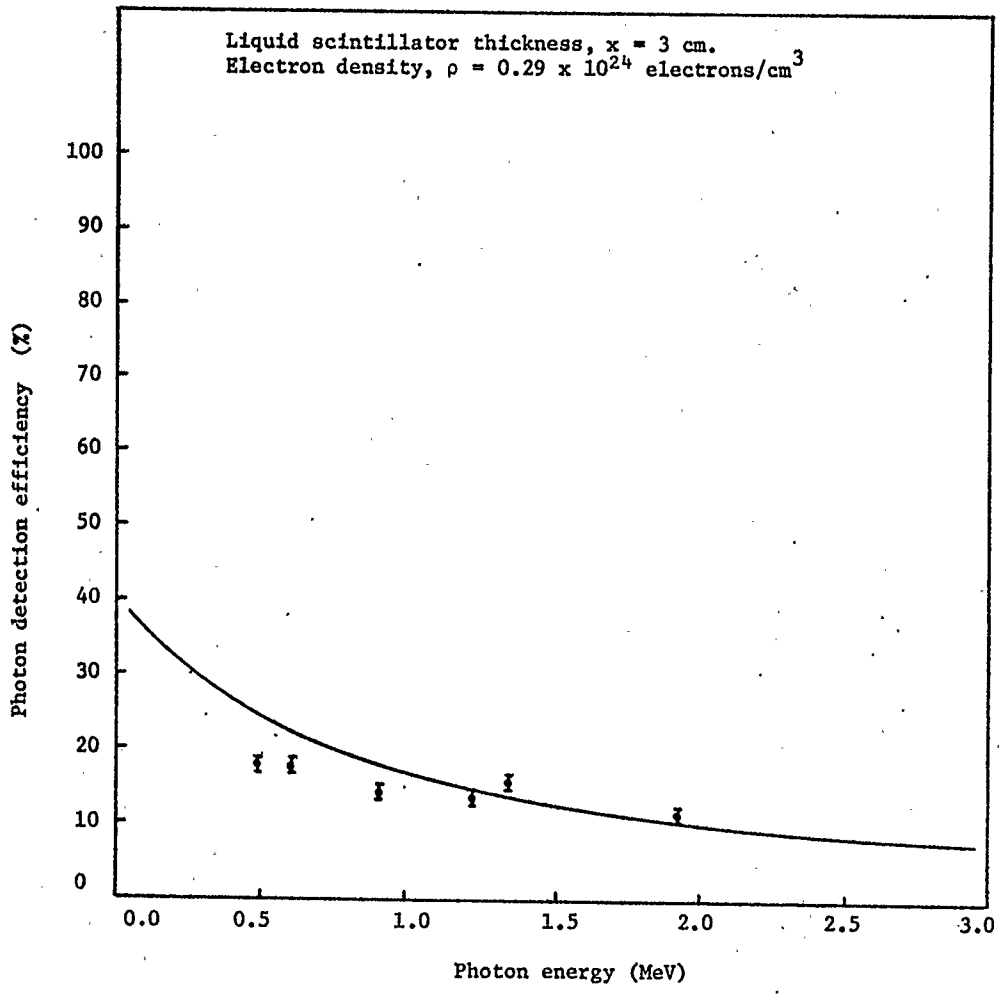

FIGURE (3-1) Photon detection efficiency of the liquid scintillator. (Line represents theoretical relation; points are measured values for various photopeaks).

CHAPTER 4

THE COMPLETE ANTICOINCIDENCE SYSTEM

4.1 Introduction

The instrumental objectives of this experiment have been determined by the sample-analysis objective of measuring dilute concentrations of K^{40}, U^{238}, and Th^{232} elements in geological samples. The spectrometer energy resolution and stability have been discussed in Section 1.5. It was seen in Chapter 2 that the background of 20,000 cpm produced by local environmental radiation could be reduced to a cosmic-ray produced level of approximately 1200 c.p.m. by the iron shielding. In order to further increase the spectrometer signal-to-noise ratio, a liquid scintillator of approximately 20% photon detection efficiency in the 0.1 to 3 MeV region has been connected in anticoincidence with the NaI(Tl) detector. It is now necessary to optimize the performance of the anticoincidence system. A schematic diagram of the system is presented in Figure (4-1).

An early attempt to reduce the cosmic-ray background contribution of a gamma-ray spectrometer (Perkins, Nielsen, and Drebel, 1960) consisted of a 26 in. diameter by 30 in. high plastic scintillator and lead shielding surrounding a 5 in. x 5 in. NaI(Tl) crystal. This anticoincidence system resulted in background reductions of a factor of 2 to 5 in the energy region below 3 MeV. This system was improved (Nielsen and Perkins, 1967), and the total background above 0.030 MeV was 120 counts/min.

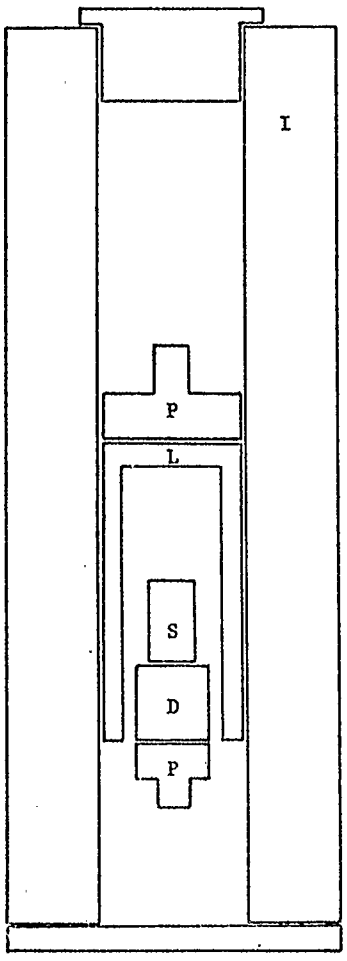

FIGURE (4-1) Schematic diagram of the spectrometer.
I = Iron shielding,
D = NaI(Tl) detector
L = Liquid scintillator
S = Sample
P = Photomultiplier

4.2 The Anticoincidence Circuit Logic

An anticoincidence circuit implements the following logical statements: if A = 1, B = 1, ..., M = 1, and if N = 0, then Y = 1. However, if N = 1, then the coincidence of A, B, ..., M is inhibited and Y = 0. The Boolean expression for this circuit (Chaing, 1969) is

$$Y = A \text{ and } B \text{ and } \ldots \text{ and } M \text{ and not } N \tag{4-1}$$

or

$$Y = AB \ldots M\overline{N}$$

In this experiment, A represents the NaI(Tl) detector, and B represents the liquid scintillator, so that the logic statement is

$$Y = A\overline{B} \tag{4-2}$$

The truth table is given in Table (4-1).

4.3 Electronics

The block diagram of the electronics is shown in Figure (4-2). A high voltage supply (Fluke 412B) operated at 1300V provides a stable source of power for the photomultiplier. The scintillator is optically coupled to an EMI 9732 photomultiplier tube from which pulses are fed to an emitter follower. The output from this amplifier produces the signal input of the anticoincidence gate. These pulses are in the range 0.1 to 10V and have a width of approximately 1μ sec. with a rise time of 0.2μ sec.

Power for the liquid scintillator is provided by a Canberra 3002 high voltage supply operated at 1800V. The liquid

TABLE (4-1)

Anticoincidence Circuit Truth Table

Input		Output
A	B	Y
0	0	0
0	1	0
1	0	1
1	1	0

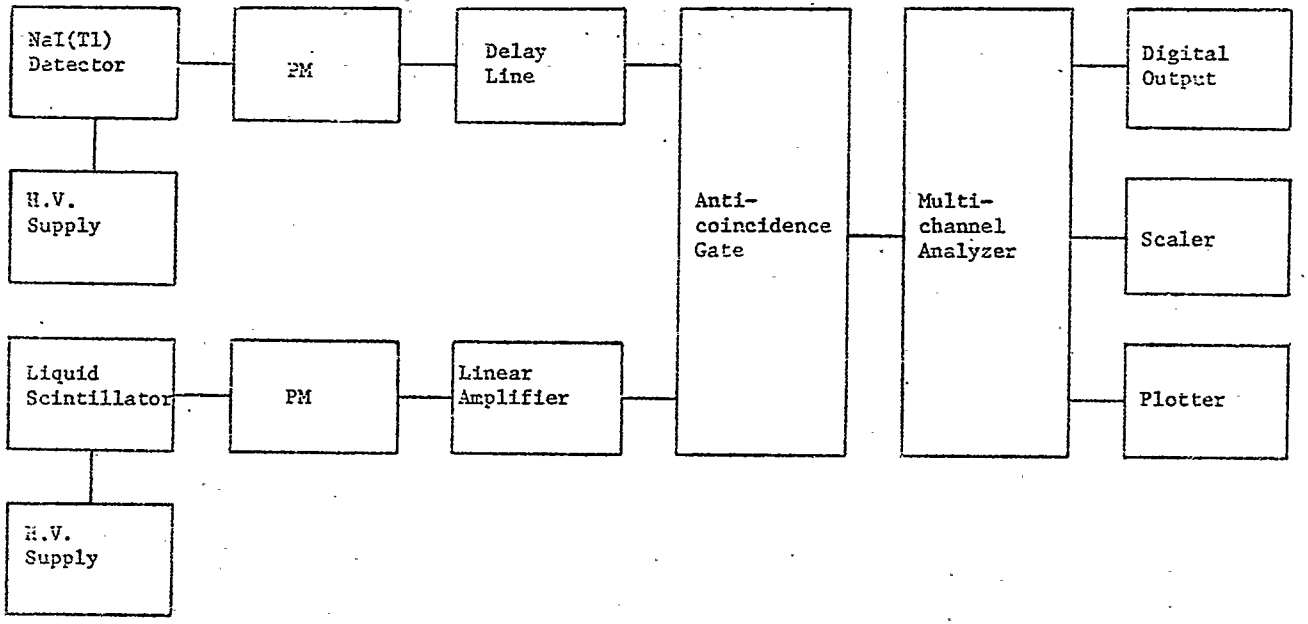

FIGURE (4-2) Block diagram of the electronics.

scintillator is coupled to an EMI 9623B photomultiplier which produces pulses of - 0.5V and 0.2μ sec width. In order to obtain sufficient voltage to trigger the anticoincidence gate the output of the photomultiplier tube is fed to a linear amplifier and single channel analyzer (Nuclear Enterprises 4630). The amplifier output, 7V, 1μ sec width, and 0.1μ sec rise time is fed to the anticoincidence gate input.

When pulses from the NaI(Tl) detector and liquid scintillator are coincident within the gate width, which can be varied from 1 to 10 μ sec, the detector pulses are inhibited by the anticoincidence circuit. When pulses from the detector arrive at the anticoincidence signal input during an interval in which they are not coincident with liquid scintillator pulses, they are fed to the low input of the Laben 400 channel analyzer. The amplifier course gain was set at the direct level. The remaining analog-to-digital settings were 20mV/channel, a back bias of 0.00, and an upper threshold of 10.00.

In order to match the high impedance of the photomultiplier output to the low impedance of the connecting cable, an emitter follower was used. The emitter follower and its T-equivalent circuit are shown in Figure (4-3). The current gain between the collector and base, β, has a typical value of 100. The base and emitter resistances are $r_b \simeq 400$ ohm and $r_e \simeq 40$ ohm; the output is measured across R_e. The equation governing operation is (Delaney, 1969)

$$v_{in} = i_b r_b + (\beta+1) i_b (r_e + R_e) \qquad (4-3)$$

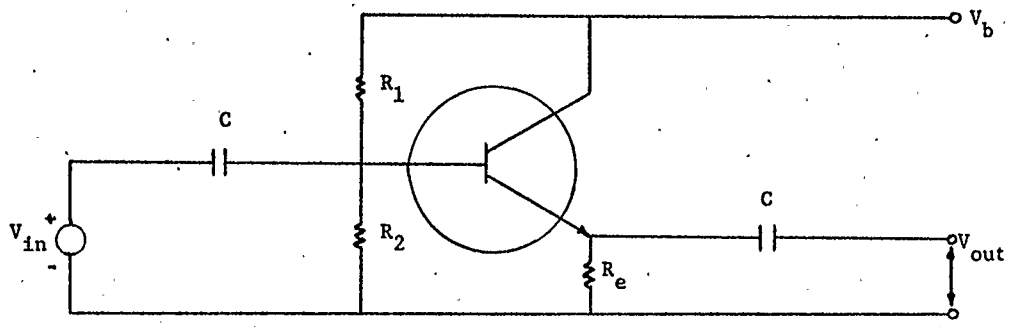

R_1 = 47K, R_2 = 22K, R_e = 1.5K, C = 0.18μF

(a)

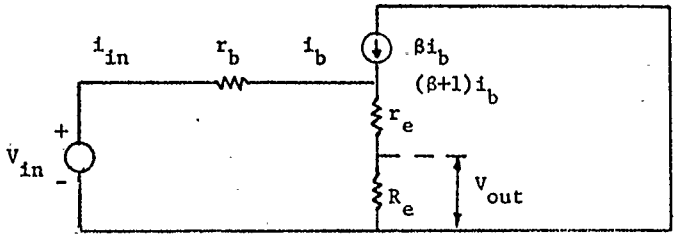

(b)

FIGURE (4-3) (a) Emitter follower,
(b) T-equivalent circuit.

giving

$$i_b = \frac{v_{in}}{r_b + (\beta+1)(r_e + R_e)} \tag{4-4}$$

A current $(\beta+1)i_b$ flows through R_e so the output voltage is $(\beta+1)i_b R_e$ and the voltage gain is

$$A = \frac{V_{out}}{V_{in}} = \frac{(\beta+1)R_e}{r_b + (\beta+1)(r_e + R_e)} \tag{4-5}$$

Recalling the relative sizes of these quantities, it is seen that the voltage gain is nearly unity.

The output impedance is $V_{out} \simeq V_{in}$ divided by $(\beta+1)i_b$, where the value of i_b is obtained from Equation (4-4) with $R_e = 0$. Thus

$$Z_{out} = \frac{r_b + (\beta+1)r_e}{(\beta+1)} = r_e + \frac{r_b}{(\beta+1)} \tag{4-6}$$

The input impedance is

$$Z_{in} = \frac{V_{in}}{i_{in}} = \frac{V_{in}}{i_b} = r_b + (\beta+1)(r_e + R_e) \simeq \beta R_e \,. \tag{4-7}$$

4.4 Optimization of the Spectrometer

Optimization of the anticoincidence spectrometer was attained by considering the factor

$$Q = \frac{\varepsilon}{B} \tag{4-8}$$

as a function of the NaI(Tl) signal delay time. The term ε represents the efficiency of the liquid scintillator in reducing the background

contribution to the spectrum in the 0.1 to 3 MeV range. This efficiency is defined as

$$\varepsilon = \frac{A-B}{A} \qquad (4-9)$$

where A is the number of background events recorded per unit time by the NaI(Tl) detector when the gate input of the anticoincidence unit is disconnected; B is the number of these events recorded when the gate input was connected and when the signal delay time was adjusted in increments of 0.1 μs. Background events were counted for a period of one hour and the values of ε, B, and Q are shown in Figure (4-4). The maximum efficiency is seen to be approximately 14% and occurs at signal delay time of 1.0 μs. This interval was adopted for subsequent sample analyses.

Integrated background counting rates of the NaI(Tl) detector under various conditions are summarized in Table (4-2). The crystal when placed outside the iron shield experienced a rate of about 2×10^4 c.p.m. The iron shielding alone reduced this rate to 1204 ± 4 c.p.m., and the iron shielding plus the liquid scintillator anticoincidence system reduced the background to 1037 ± 4 c.p.m. The effect of the anticoincidence system on the background spectrum is illustrated in Figure (4-5).

4.5 Conclusions

The optimized anticoincidence system is seen to have reduced the integrated background spectrum from 1204 ± 4 c.p.m. without anticoincidence to 1037 ± 4 c.p.m. with anticoincidence, a reduction of 14% in the 0.1 to 3 MeV region. Because the liquid

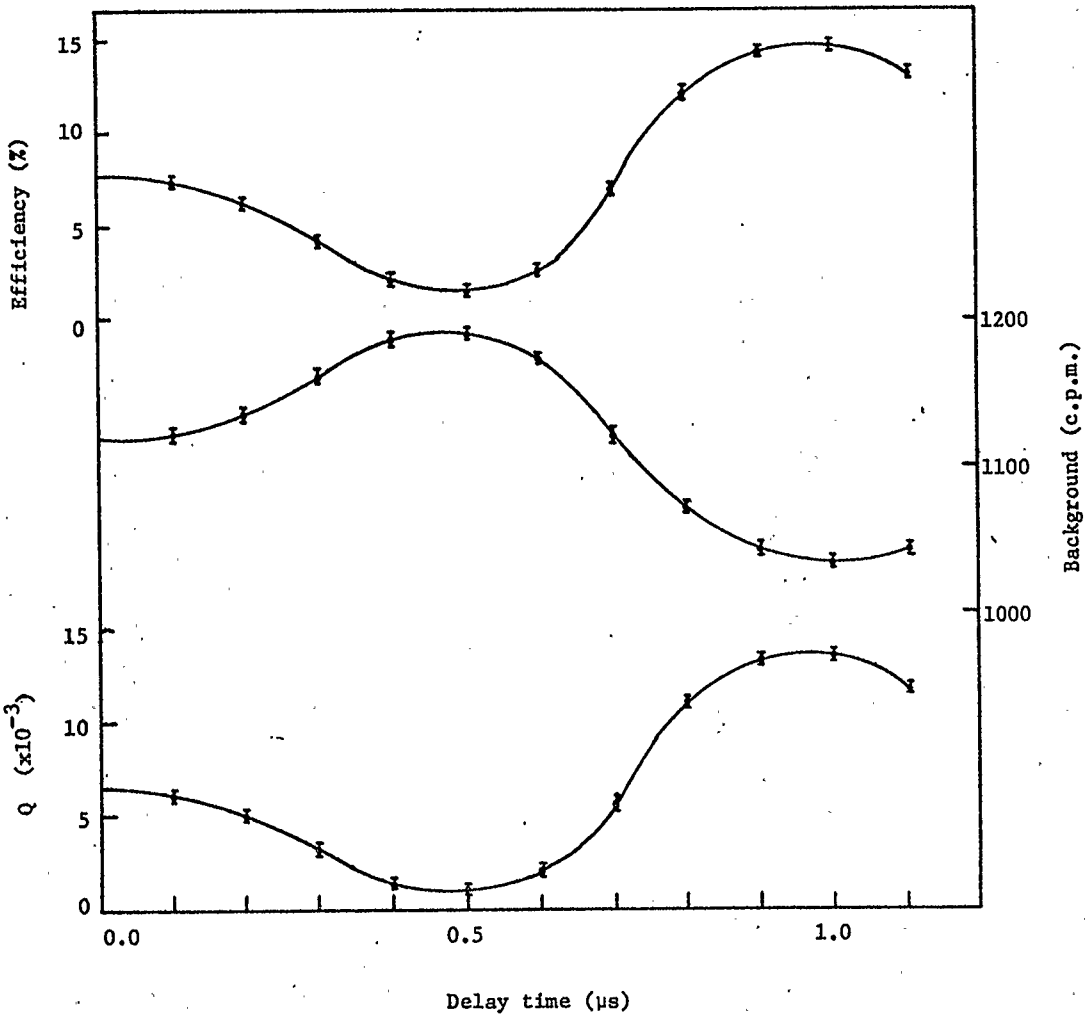

FIGURE (4-4) Effect of delay time on efficiency and background.

TABLE (4-2)

Background counting rate of the 4 in. x 4 in. Na(Tl) crystal under various conditions. Integral counting rates between 0.1 and 3 MeV are given.

Shielding	Background
Crystal outside iron shielding	2×10^4 (approx)
Crystal inside iron shielding without anticoincidence	1204±4
Crystal inside iron shielding with anticoincidence	1037±4

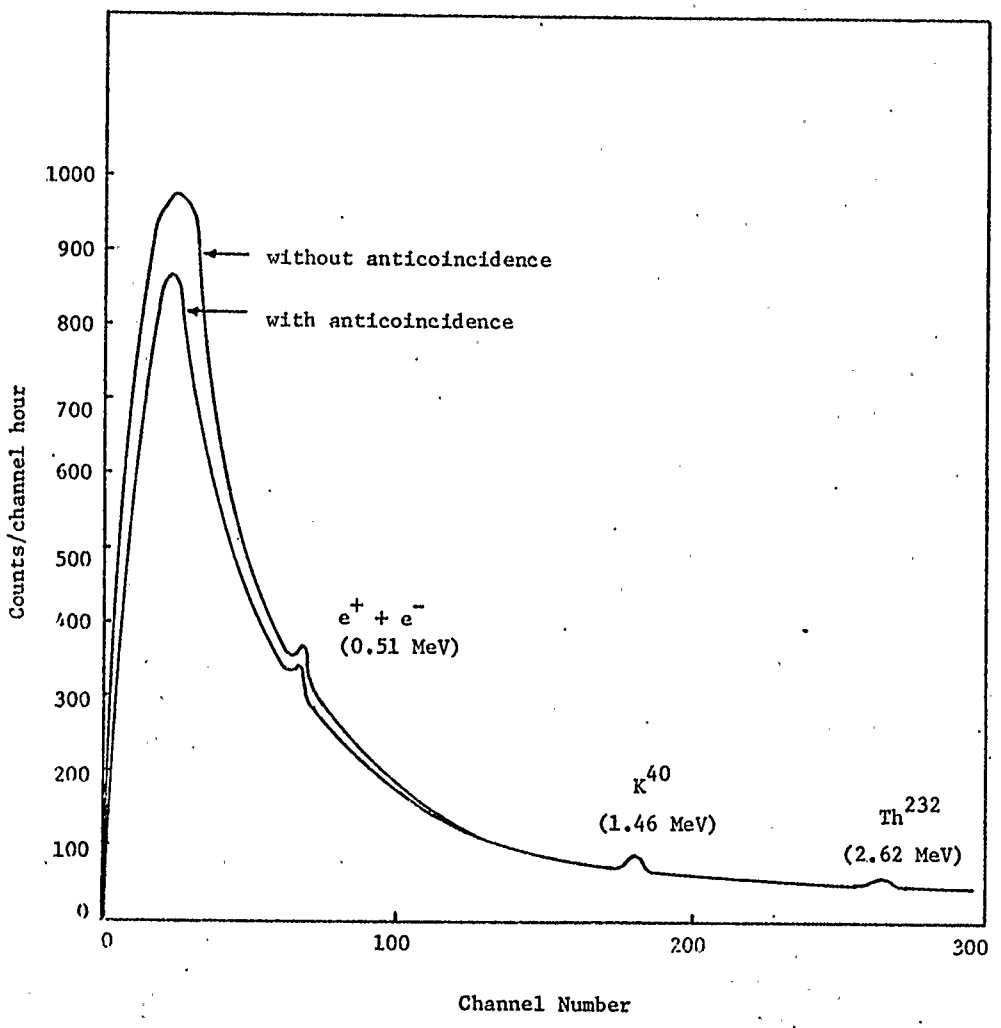

FIGURE (4-5) Effect of anticoincidence system on background spectrum.

scintillator subtends a solid angle of approximately 2π ster., the efficiency of a 4π ster. liquid scintillator in reducing the background radiation is twice the above reduction or 28%. This value agrees reasonably well with the photon detection efficiency of the liquid scintillator in the 0.1 to 3 MeV range as discussed in Chapter 3. From Chapter 2, it was determined that a cosmic ray muon interacting with a 4 in. x 4 in. NaI(Tl) crystal will produce a pulse only above 20 MeV. Also, cosmic ray muons and nucleons which interact with the iron shielding will result in many low energy electrons and photons which will be detected by the NaI(Tl) crystal. Thus, the background spectrum is primarily a result of low energy photons which have been produced by interactions of cosmic ray muons and nucleons with the iron shield.

CHAPTER 5

GAMMA RAY SPECTROMETRY OF SAMPLES

5.1 Introduction

The measurement of thorium, uranium, or thorium-to-uranium ratios in rocks and minerals is necessary in order to understand the geochemistry of these elements. For such investigations as radioactive dating (Faul, 1954), the heat balance of the earth's crust (Birch, 1954), and the rate of sedimentation (Koczy, 1954), very low concentrations of thorium and uranium must be measured in many samples. These concentrations were first measured by gamma-ray spectrometry (Hurley, 1956), where thorium and uranium were in secular equilibrium with their decay products, and where the uranium content exceeded 0.01 per cent. More sensitive measurements were obtained (Adams, 1958) when larger NaI(Tl) crystals, heavy shielding and more stable instruments allowed concentrations of about one part per million to be recorded. Through the utilization of a liquid scintillator anticoincidence system, it has been the objective of this project to increase the sensitivity of the spectrometer in the 0.1 to 3 MeV region and to determine the optimum analysis time for geological samples.

5.2 Spectrometry of Geological Samples

In order to calculate the concentration of the radioactive elements K^{40}, U^{238}, and Th^{232} in a geological sample by integrating the K^{40} photopeak at 1.46 MeV, the Bi^{214} photopeak at 0.61 MeV, and the Tl^{208} photopeak at 2.62 MeV, it is necessary to consider the

conditions required for secular equilibrium. At any time, t, let N_1 be the number of atoms of the parent element which decays with a decay constant λ_1 into its daughter element. Let N_2 be the number of atoms of the daughter element which further decays with a decay constant λ_2 into a stable element with N_3 stable atoms. Next, assume that at $t = 0$, $N_1 = N_{10}$, $N_2 = N_{20} = 0$, and $N_3 = N_{30} = 0$. The decay series will then proceed as

$$\frac{dN_1}{dt} = -\lambda_1 N_1 \tag{5-1}$$

$$\frac{dN_2}{dt} = \lambda_1 N_1 - \lambda_2 N_2 \tag{5-2}$$

$$\frac{dN_3}{dt} = \lambda_2 N_2 \tag{5-3}$$

The solution for N_2 is given (Arya, 1966) as

$$N_2 = \frac{\lambda_1}{\lambda_2 - \lambda_1} N_{10} \left(e^{-\lambda_1 t} - e^{-\lambda_2 t}\right) . \tag{5-4}$$

When the half-life of the parent is very long compared to that of its daughter, $\lambda_1 << \lambda_2$ then Equation (5-4) becomes

$$N_2 = \frac{\lambda_1}{\lambda_2} N_{10} \left(1 - e^{-\lambda_2 t}\right) . \tag{5-5}$$

If t is much larger than the mean life of the daughter, that is $t >> 1/\lambda_2$, then

$$N_2 = \frac{\lambda_1}{\lambda_2} N_{10} \tag{5-6}$$

which means that the amount of the daughter, N_2, is constant; in this case the daughter is said to be in permanent or secular equilibrium with the parent element. Since the half-life of the parent is large, $N_{10} = N_1$, and

$$\lambda_1 N_1 = \lambda_2 N_2 \tag{5-7}$$

which is the condition for secular equilibrium. For the case of many successive decays in which the parent has a much longer half-life than any of its decay products, the condition for secular equilibrium is

$$\lambda_1 N_1 = \lambda_2 N_2 = \lambda_3 N_3 = \ldots = \lambda_n N_n \ . \tag{5-8}$$

K^{40} is the only unstable isotope of potassium, and it occurs with a natural isotopic abundance of 1.18×10^{-4}. The decay scheme of K^{40} is illustrated in Figure (5-1) in which the isotope undergoes branched decay by e^- emission to Ca^{40} or, mostly by electron capture, to Ar^{40}. The radioactive properties of K^{40} are given in Table (5-1). The decay constant for β^- emission is $\lambda_{\beta^-} = 1.50 \times 10^{-17}$ sec^{-1} while that for electron capture is $\lambda_{E.C.} = 0.18 \times 10^{-17}$ sec^{-1} producing a total decay constant of 1.68×10^{-17} sec^{-1} and a branching ratio of 11.7%. The process of β^- emission occurs when K^{40} decays directly to Ca^{40} in the ground state; electron capture leaves the Ar^{40} nucleus in an excited state from which a 1.46 MeV photon is emitted.

The Th^{232} decay series is shown in Table (5-2). The relatively short half-life of all decay products allows for

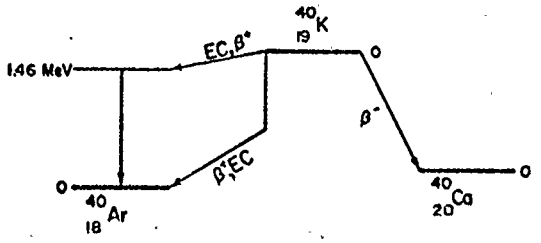

FIGURE (5-1) Decay scheme of K^{40} (From Adams and Gasparini, 1970).

TABLE (5-1)

RADIOACTIVE CONSTANTS OF K^{40}

Decay mode	Branching ratio	Half-life (years)	Decay Constant (sec^{-1})	Radiation	Energy (MeV)	Absolute intensity (%)
e^- emission	0.89	1.47×10^9	1.05×10^{-17}	e^-	1.31 (max.)	89
Electron capture	0.11	1.18×10^{10}	0.18×10^{-17}	γ	1.46	11

From Adams and Gasparini, 1970.

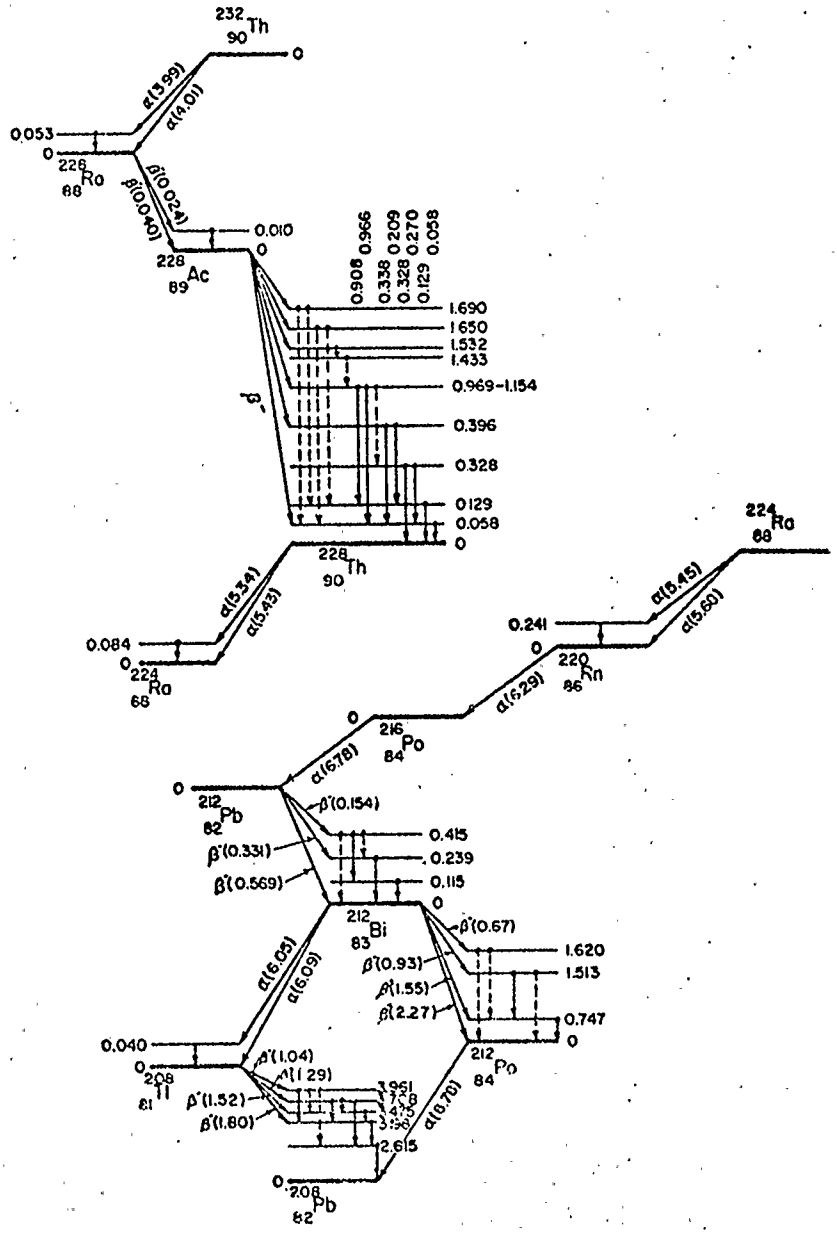

FIGURE (5-2) Decay scheme of the Th^{232} series. (From Adams and Gasparini, 1970).

TABLE (5-2)

Th^{232} Series

Isotope	*Classical name*	$T_{\frac{1}{2}}$	$\lambda(sec^{-1})$	*Primary decay mode*	*Remarks*
$^{232}_{90}Th$	Thorium	$1.41 \cdot 10^{10}$ yr	$1.56 \cdot 10^{-18}$	α	
$^{228}_{88}Ra$	Mesothorium 1	6.7 yr	$3.28 \cdot 10^{-9}$	β^-	
$^{228}_{89}Ac$	Mesothorium 2	6.13 h	$3.14 \cdot 10^{-5}$	β^-	
$^{228}_{90}Th$	Radiothorium	1.910 yr	$1.15 \cdot 10^{-8}$	α	
$^{224}_{88}Ra$	Thorium X	3.64 days	$2.21 \cdot 10^{-6}$	α	
$^{220}_{86}Rn$	Thoron	55.3 sec	$1.25 \cdot 10^{-2}$	α	
$^{216}_{84}Po$	Thorium A	0.145 sec	4.78	α	
$^{212}_{82}Pb$	Thorium B	10.64 h	$1.81 \cdot 10^{-5}$	β^-	
$^{212}_{83}Bi$	Thorium C	60.60 min	$1.91 \cdot 10^{-4}$	α, β^-	branched decay: β^- (66.3%) to ^{212}Po α(33.7%) to ^{208}Tl
$^{212}_{84}Po$	Thorium C'	$3.04 \cdot 10^{-7}$ sec	$2.28 \cdot 10^{6}$	α	
$^{208}_{81}Tl$	Thorium C''	3.10 min	$3.73 \cdot 10^{-3}$	β^-	
$^{208}_{82}Pb$	Thorium D	stable			

(From Adams and Gasparini, 1970)

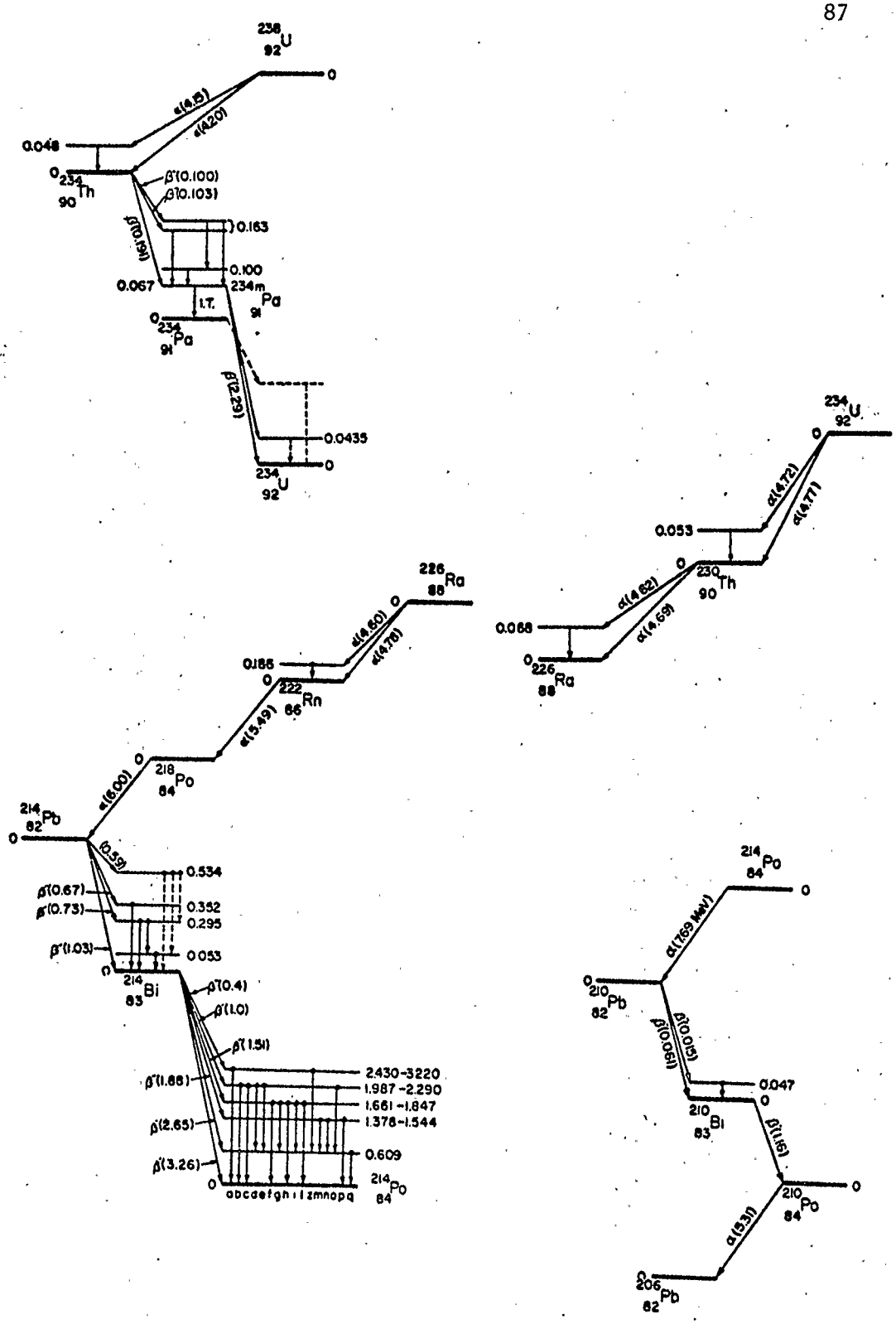

FIGURE (5-3) Decay scheme of the U^{238} series. (From Adams and Gasparini, 1970).

TABLE (5-3)

U^{238} Series

Isotope	*Classical name*	$T_{\frac{1}{2}}$	$\lambda(sec^{-1})$	*Primary decay mode*	*Remarks*
$^{238}_{92}U$	Uranium I	$4.51 \cdot 10^{9}$ yr	$4.88 \cdot 10^{-18}$	α	
$^{234}_{90}Th$	Uranium X_1	24.10 days	$3.33 \cdot 10^{-7}$	β^-	
$^{234m}_{91}Pa$	Uranium X_2	1.175 min	$9.83 \cdot 10^{-3}$	β^-	isomeric transition to ^{234}Pa (0.13%)
$^{234}_{91}Pa$	Uranium Z	6.75 h	$2.85 \cdot 10^{-5}$	β^-	
$^{234}_{92}U$	Uranium II	$2.47 \cdot 10^{5}$ yr	$8.91 \cdot 10^{-14}$	α	
$^{230}_{90}Th$	Ionium	$8.0 \cdot 10^{4}$ yr	$2.75 \cdot 10^{-13}$	α	
$^{226}_{88}Ra$	Radium	1,602 yr	$1.37 \cdot 10^{-11}$	α	
$^{222}_{86}Rn$	Radon	3.8223 days	$2.10 \cdot 10^{-6}$	α	
$^{218}_{84}Po$	Radium A	3.05 min	$3.79 \cdot 10^{-3}$	α, β^-	branched decay: α to ^{214}Pb (99.98%); β^- to ^{218}At (0.02%)
$^{214}_{82}Pb$	Radium B	26.8 min	$4.31 \cdot 10^{-4}$	β^-	
$^{218}_{85}At$	Astatine-218	~2 sec	~0.35	α	
$^{214}_{83}Bi$	Radium C	19.7 min	$5.86 \cdot 10^{-4}$	α, β^-	branched decay: α to ^{210}Tl (0.04%); β^- to ^{214}Po (99.96%)
$^{214}_{84}Po$	Radium C'	$1.64 \cdot 10^{-4}$ sec	$4.23 \cdot 10^{3}$	α	
$^{210}_{81}Tl$	Radium C''	1.32 min	$8.75 \cdot 10^{-2}$	β^-	
$^{210}_{82}Pb$	Radium D	22.0 yr	$1 \cdot 10^{-9}$	β^-	branched decay: α to ^{206}Hg ($1.8 \cdot 10^{-6}$%) β^- to ^{210}Bi (~100%)
$^{210}_{83}Bi$	Radium E	5.013 days	$1.60 \cdot 10^{-6}$	β^-	branched decay: α to ^{206}Tl ($\sim 10^{-5}$%) β^- to ^{210}Po (~100%)
$^{210}_{84}Po$	Radium F	138.4 days	$5.78 \cdot 10^{-8}$	α	
$^{206}_{82}Pb$	Radium G	stable			

(From Adams and Gasparini, 1970)

achievement of secular equilibrium in natural systems after about 40 years. The decay scheme po Th^{232} is shown in Figure (5-2).

Table (5-3) presents the decay series of U^{238}. The long lived decay products U^{234}, Th^{230}, and Ra^{226} result in the requirement of a period of 10^4 to 10^6 years for the establishment of secular equilibrium. The U^{238} decay scheme appears in Figure (5-3).

5.3 Analysis of the Spectra

As an example of geological gamma ray spectrometry, five samples obtained from Great Canadian Oil Sands Limited of Fort McMurray, Alberta were analyzed. Assuming secular equilibrium of the U^{238} and Th^{232} decay products, concentrations of these elements as well as that of K^{40} were determined. The calculation of concentration begins by measuring the net counts (total counts minus background counts) for each photopeak of the spectrum. Figure (5-4) illustrates such a spectrum.

Before explaining the method of analyzing the gamma ray spectra, it is necessary to define the term "photopeak." From Chapter 1 it was seen that the peak resulting from total energy loss of the incident photon is the photopeak. Although the incident beam of photons is monoenergetic, for a given decay process, the photopeak is broadened due to fluctuations in the number of visible scintillation photons produced and to the variance of processes occurring in the photomultiplier. The width of this peak is a measure of the energy resolution of the detector. For a quantitative analysis of the spectra this width must be well established.

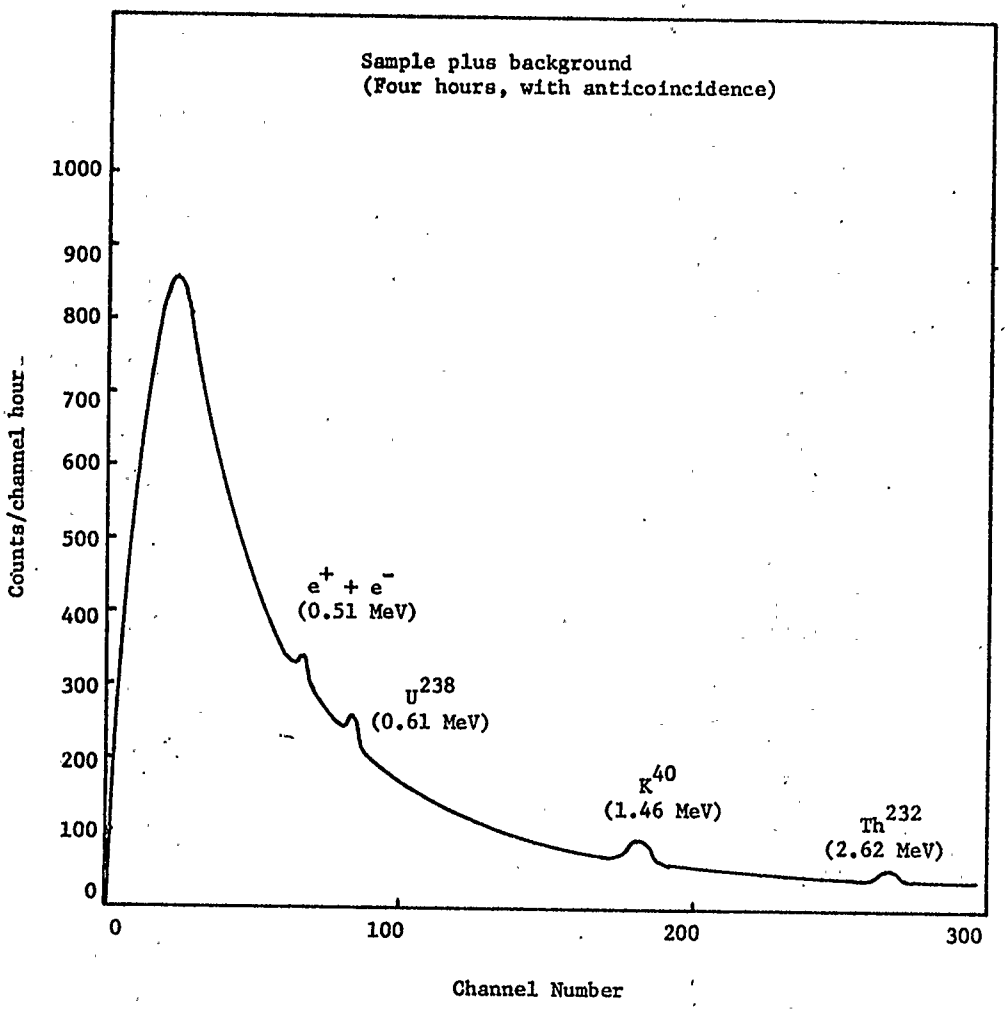

FIGURE (5-4) Spectrum of GCOS 1300-2 sample.

Several methods have been developed for the quantitative reduction of gamma ray spectra. The weighted least squares method (Ryback et al., 1966) was used to measure Mont-Blanc granite samples which contain uranium and thorium concentrations of 4 to 20 ppm and 10 to 60 ppm respectively. The samples were counted for 1000 seconds and the signal-to-noise ratio was greater than 20 over the entire spectrum. This analysis fits a polynomial through the experimental data points and calculates the sample concentrations by comparing the sample spectrum with spectra produced by standards of known concentrations. An attempt was made to adapt this procedure for the spectra analyses. However, as a result of the low concentration of K^{40}, U^{238}, and Th^{232} in the samples measured, the signal-to-noise ratio of all photopeaks was less than 0.5, and the solutions of the normal equations were erroneous.

Another method (Bevington, 1969) fits a Gaussian peak on a quadratic-polynomial background according to the relation

$$y(x) = a_1 \exp\left[-\frac{1}{2}\left(\frac{x-a_2}{a_3}\right)^2\right] + a_4 + a_5 x + a_6 x^2 . \qquad (5\text{-}9)$$

However, the background spectra recorded during this experiment contain, in addition to the slowly varying component, photopeaks caused by the impurities K^{40}, U^{238}, and Th^{232} in the detector and shielding. Thus, in order to obtain the net photopeak counting rate, Gaussian peaks would be required for both the total (i.e., sample plus background) spectrum and the background spectrum.

The procedure initially used to determine the photopeak width was to first locate, in the sample-plus-background spectrum,

the channel containing the maximum number of counts, i_o, as in Figure (5-5). Then, the minimum-energy channel, -i, was found. This was done by observing that the intensity of the background spectrum increases fairly uniformly with decreasing energy. The background spectrum is also approximately linear over a short interval with superimposed photopeaks due to the impurities K^{40}, U^{238}, and Th^{232} in the detector and shielding. Channel -i thus occurs where the counting rate on the lower energy side of i_o is a minimum. If the background were constant with energy, the Gaussian photopeak would by symmetric about i_o and the interval -i to i_o would be equivalent to the interval i_o to +i. This equality was assumed in order to establish the channel +i even though the background is not constant throughout the spectrum. It will be seen that this assumption was reasonable for the K^{40} and Th^{232} photopeaks, while not as valid for the U^{238} peak.

To verify the accuracy of determining the photopeak width from the sample-plus-background spectrum, the net photopeak counting rate was plotted for the same width as shown in Figure (5-6). It can be seen that the K^{40} and Th^{232} net photopeaks are approximately Gaussian while that of U^{238} is not as well defined. Assuming a Gaussian distribution for these peaks, the channel containing the maximum number of net counts is

$$i_o' = \frac{\sum_{i=1}^{m} n_i \, i}{N_{measured}} \qquad (5\text{-}10)$$

where n_i is the number of counts in channel i and $N_{measured}$ is the total

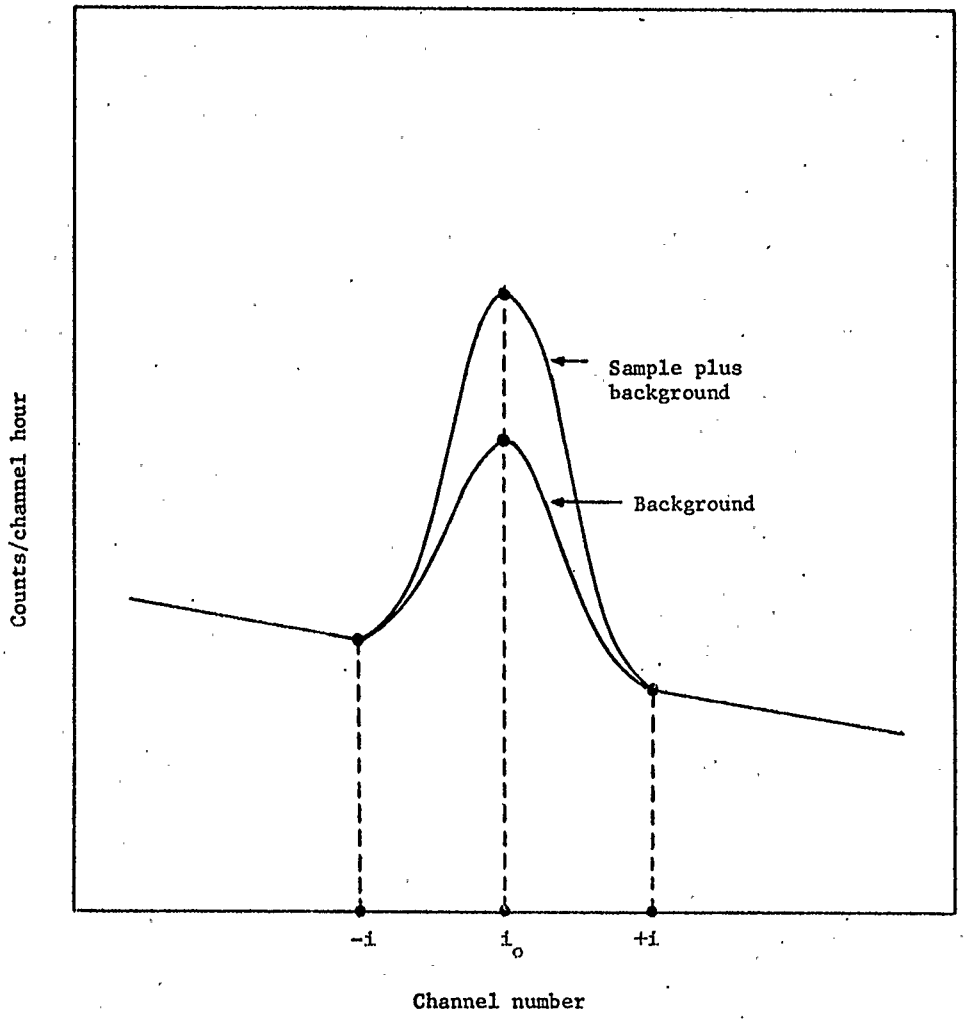

FIGURE (5-5) Schematic diagram of a photopeak.

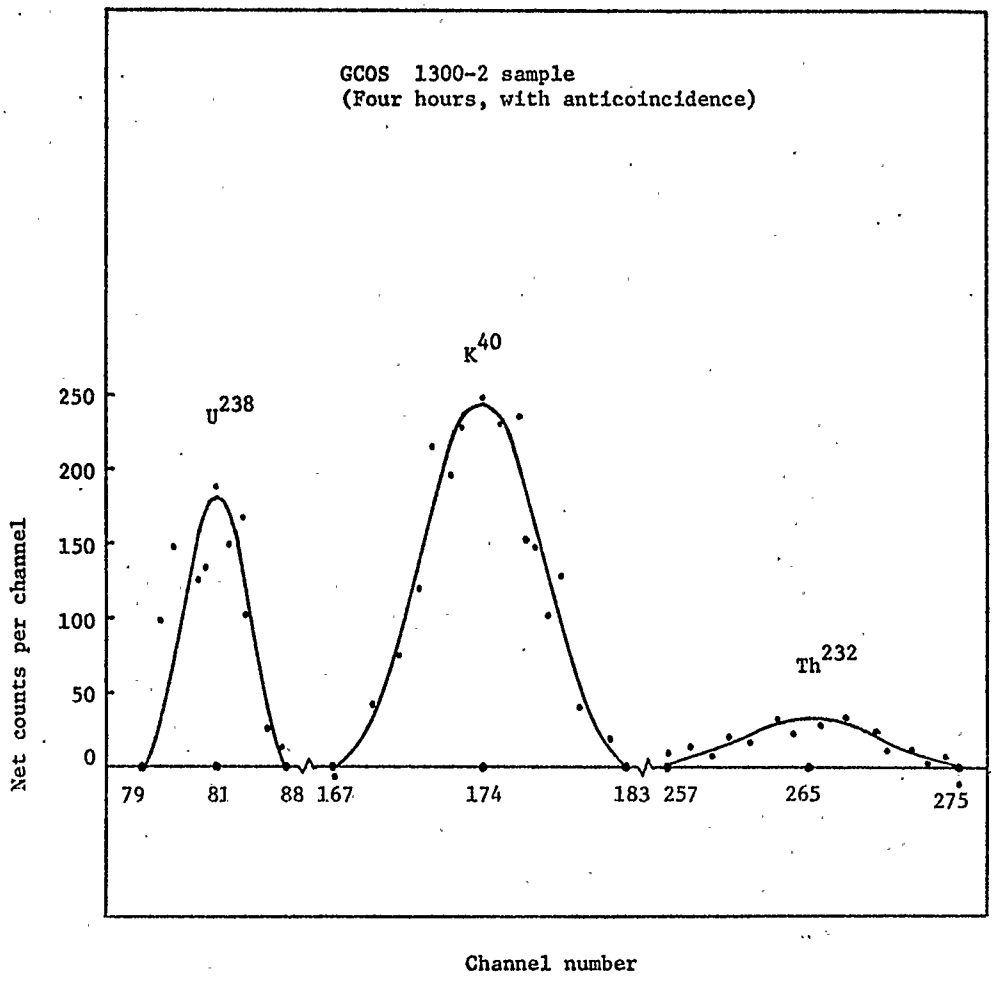

FIGURE (5-6) Net counting rates of photopeaks.

number of net counts in the photopeak of width m. The standard deviation in the number of channels from i_o' is

$$\sigma_i = \left[\frac{\sum_{i=1}^{m} n_i (i - i_o')^2}{N_{measured} - 1} \right]^{1/2} . \qquad (5\text{-}11)$$

A photopeak of half-width $2\sigma_i$ will contain 95.5% of the total number of net counts. The value of $\pm 2\sigma_i$ was used to set the limits of the photopeak width, -i' and +i'. With these limits the total number of net counts, $N_{calculated}$, was found for each photopeak. A comparison of i_o, $\pm i$, and N using the two procedures is presented in Table (5-4). The error for the K^{40} and Th^{232} photopeaks is approximately 2%. The higher counting rate and the larger negative slope of the background spectrum in the region of the U^{238} peak resulted in an error of 24%. By identification of the photopeak width, -i to +i, from the sample-plus-background spectrum, quantitative analysis of the spectra can be initiated.

The U^{238} decay product, Bi^{214} exhibits a photopeak at 0.61 MeV which occurs between channels 79 and 88 of the spectrum. The number of counts in the Bi^{214} peak is determined from the relation

$$N_{Bi} = \frac{dN_{pBi}/dt}{\lambda_{Bi}} . \qquad (5\text{-}12)$$

Similarly, the decay product Tl^{208} of the Th^{232} series has the following number of counts in the 2.62 MeV photopeak between channels 257 and 275

$$N_{Tl} = \frac{dN_{pTl}/dt}{\lambda_{Tl}} . \qquad (5\text{-}13)$$

TABLE (5-4)

COMPARISON OF PHOTOPEAK PARAMETERS

GCOS 1300-2, 4 HOURS WITH ANTICOINCIDENCE

Parameter	Method 1 Measured spectrum			Method 2 Calculated values		
	U^{238}	K^{40}	Th^{232}	U^{238}	K^{40}	Th^{232}
-i	79	167	257	77	169	257
i_o	81	174	265	83	175	265
+i	88	183	275	86	182	272
N	1278	2289	356	1587	2335	362
$\frac{N_{calculated}}{N_{measured}}$	1.24	1.02	1.02	-	-	-

Because K^{40} is a direct emitter of gamma photons, the number of counts in the 1.46 MeV photopeak in channels 167 to 183 is given by

$$N_K = \frac{dN_{pK}/dt}{\lambda_K} \quad . \tag{5-14}$$

N_{pBi}, N_{pTl}, and N_{pK} are the net number of counts for each photopeak. Recalling the relation for secular equilibrium, Eq. (5-8), the number of U^{238} and Th^{232} counts are

$$N_U = \frac{\lambda_{Bi}}{\lambda_U} N_{Bi} \tag{5-15}$$

$$N_{Th} = \frac{\lambda_{Tl}}{\lambda_{Th}} N_{Tl} \quad . \tag{5-16}$$

Corrections must then be made for series branching, absolute intensity, and geometrical efficiency. Branching occurs in the U^{238} series when Po^{218} decays by α decay to Pb^{214} (99.98%) and by e^- to At^{218} (0.02%). Similarly for the Th^{232} series, Bi^{212} decays by e^- emission to Po^{212} (66.3%) and by α decay to Tl^{208} (33.7%). The number of gamma photons of a given energy emitted per one hundred disintegrations of the parent nucleus is known as the absolute intensity. These values together with the branching ratios and the geometrical efficiencies of Section 1.6 are given in Table (5-5).

Multiplication of N_U, N_{Th}, and N_K by their respective total correction factor gives the number of counts originating from the sample. The mass of element i is then given by

$$M_i = N_i \frac{M_c}{12} A_i, \quad i = U, Th, K \tag{5-17}$$

TABLE (5-5)

SAMPLE CONCENTRATION CORRECTION FACTORS

Correction	U^{238} 0.61 MeV	K^{40} 1.46 MeV	Th^{232} 2.62 MeV
Branching = B	0.9998	-	0.337
Absolute Intensity = A	0.47	0.11	1.00
Geometrical Efficiency = M	10.78	20.99	33.77
Total Correction C = M/AB	22.94	190.81	100.21

where M_c is the mass of C^{12} in gm., and A_i is the atomic weight of U^{238}, Th^{232}, K^{39}. The sample concentration for element i is

$$C_i = \frac{M_i}{M_s} \tag{5-18}$$

where M_s is the total mass of the sample in gm. The CDC computer program for these computations and an example of the results is presented in the Appendix.

Values of C_i are given in Table (5-6). All of the oil sands samples have comparable Th^{232}/U^{238} ratios of approximately $Th^{232}/U^{238} = 4$. This value is a nominal one for ordinary rock samples which indicates that these elements are contained in the sand. The ratio of Th^{232}/U^{238} for the coke sample (GCOS C-1) is about twice that of the oil sands samples suggesting a possible leaching of U^{238}.

5.4 Counting Errors, Anticoincidence System Effectiveness, Optimum Analysis Time, and Decection Limits

The emission of gamma ray photons from a large number of nuclei in a source is a random process and can, therefore, be described by Poisson statistics. The probability, P_x, that x photons per unit time will be emitted from a number of identical nuclei is given by

$$P_x = A^x \frac{e^{-N}}{x!} \tag{5-19}$$

where N is the average number of photons emitted per unit time.

TABLE (5-6)

Concentration of GCOS samples for four hour counting time.

Sample	Sample size (gm)	Concentration			
		K^{39} (gm/gm) $\times 10^{-3}$	U^{238} (gm/gm) $\times 10^{-7}$	Th^{232} (gm/gm) $\times 10^{-6}$	Th^{232}/U^{238}
GCOS 1300-1	367	2.20 ± 0.03	6.57 ± 0.31	2.72 ± 0.08	4.1
GCOS 1300-2	385	2.71 ± 0.05	4.60 ± 0.36	1.95 ± 0.24	4.2
GCOS 1301-1	355	2.24 ± 0.09	2.57 ± 0.37	1.09 ± 0.24	4.2
GCOS 1301-2	393	2.62 ± 0.14	7.63 ± 0.30	2.69 ± 1.10	3.5
GCOS C-1	262	negligible	2.04 ± 0.45	1.96 ± 0.08	9.6

The counting error is expressed as the standard deviation

$$\sigma = n^{\frac{1}{2}} \tag{5-20}$$

where n is the total number of counts in the photopeak. When the counting error is expressed as a standard deviation, the probability is 68.3% that the correct value is within one standard deviation; 2σ increases this probability to 95.5%, and 3σ increases the probability to 99.7%.

The total number of counts recorded in the photopeak, t, is the sum of the counts from the source, s, plus the counts from the background, b. For this case (Loevinger and Berman, 1951) the standard deviation of the sample counts is

$$\sigma_s = (\sigma_t^2 + \sigma_b^2)^{\frac{1}{2}} . \tag{5-21}$$

The sample error can be defined in terms of the coefficient of variation

$$V_s = \frac{\sigma_s}{N_s} \tag{5-22}$$

and can be expressed in an alternative form using Equations (5-17) and (5-18) as

$$V_s = \frac{(N_t + N_b)^{\frac{1}{2}}}{(N_t - N_b)} . \tag{5-23}$$

Counts are accumulated at the rate of $R = N/T$, so that for the case of $T_t = T_b$, Equation (5-20) becomes in per cent

$$V_s = 100 \frac{(R_t + R_b)^{\frac{1}{2}}}{(R_t - R_b)} \frac{1}{T_t^{\frac{1}{2}}} \quad . \qquad (5\text{-}24)$$

Writing the ratio of the total counts to the background counts as $r = R_t/R_b$, Equation (5-21) is then

$$V_s = 100 \frac{(r + 1)^{\frac{1}{2}}}{(r - 1)} \frac{1}{(R_b T_t)^{\frac{1}{2}}} \quad . \qquad (5\text{-}25)$$

For a given sample-detector configuration, R_t and R_b will remain constant, and V_s will asymptotically approach zero as $T_t^{-\frac{1}{2}}$. However, even if instrumental drift does not tend to increase V_s after a certain counting period, a reduction in V_s of only 1% may require a doubling of the counting interval which could be economically unjustified. Figure (5-7) illustrates the effect of counting time on decreasing the sample per cent error for 385 gm. of the GCOS 1300-2 sample in which the curves were calculated from Equation (5-22).

A measurement of the effectiveness of the anticoincidence system in reducing the background is the value of r for each of the photopeaks. As seen from Table (5-7) the increase in r produced by this system is 2.6%, 2.4%, and 2.5% for the K^{39}, U^{238}, and Th^{232} photopeaks respectively. This marginal increase in r is also illustrated in Figure (5-7) where it is evident that the anticoincidence system did not significantly reduce the sample error.

As shown in Section 1.5, the spectrometer is stable (a ± 1 channel drift) for at least 15 hours. Therefore, an increase in sample error due to instrumental drift should not be expected for

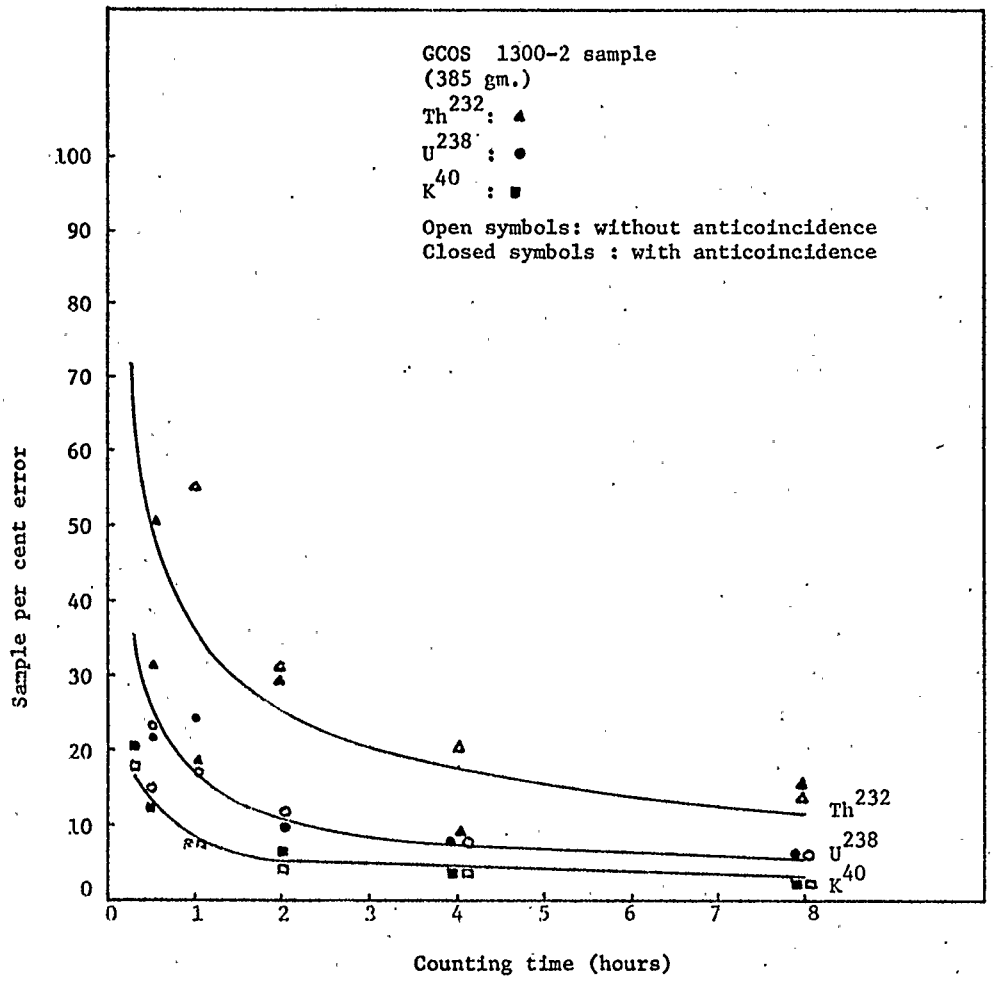

FIGURE (5-7) Effect of counting time on sample per cent error.

TABLE (5-7)

Effect of the anticoincidence system in reducing photopeak background. The value of $r = R_t/R_b$ is given for each photopeak.

	K^{39} (K^{40})	U^{238} (Bi^{214})	Th^{232} (Tl^{208})
With anticoincidence	1.545	1.167	1.224
Without anticoincidence	1.505	1.140	1.193

this period. As only a few per cent reduction in sample error is recorded for counting intervals exceeding four hours, this time appears to be an optimum when measuring 1 kg. samples.

Assigning the value of 2σ as the detection limit (95% confidence level), the limits for the GCOS elements K^{39}, U^{238}, and Th^{232} are 0.18×10^{-3} gm./gm., 0.64×10^{-7} gm./gm., and 0.38×10^{-6} gm./gm. respectively after a four-hour measurement.

5.5 Summary and Final Conclusions

Measurements of low concentrations of the radioactive elements potassium, uranium, and thorium require several instrumentational parameters in addition to sensitivity. It was evident from Section 1.5 that the spectrometer possesses reasonable linearity in the range of 0.1 to 2.62 MeV. The overall stability of the instrument, including the high voltage power supply, photomultiplier, and multichannel analyzer is ±1 channels during a 15 hour period. This interval is considerably longer than the optimum analysis time of 4 hours for a 1 kg. sample. The spectral resolution, 9.1% for the standard 0.662 MeV Cs-137 source, is adequate to resolve the high absolute-intensity photopeaks of K^{40}, B^{214}, and Tl^{208} but is insufficient to distinguish the 0.61 MeV peak of Bi^{214} from the 0.65 MeV peak of Rn^{224}. The calculated geometrical efficiency for cylindrical samples proved to be in error by about 5%. This error, while intolerable for concentrated samples, will usually be less than the statistical sample error for dilute samples.

The NaI(Tl) detector registered approximately 20,000 c.p.m. when placed outside the iron shield but inside the laboratory as a result of environmental radioactive contaminants. This background

flux was reduced to 1204±4 c.p.m. when the detector was placed inside the shield.

The measured photon detection efficiency of the liquid scintillator agreed reasonably well with the theoretical values and was found to be nearly constant at 20% in the 0.5 to 3 MeV region. A scintillator thickness of 22 cm. would increase this efficiency to 99%.

Optimization of the anticoincidence system was obtained by delaying the NaI(Tl) detector pulse 1.0 μsec; the background flux was then reduced from 1204 ± 4 c.p.m. to 1037 ± 4 c.p.m., a reduction of 14% for 2π steradian geometry. This reduction is approximately the same as the photon detection efficiency of the liquid scintillator and allows the background radiation to be identified primarily as photons which are produced by the interaction of cosmic ray muons and nucleons with the iron shield. This minimum background of about 1000 c.p.m. can be compared with the best spectrometer found in the literature which produces about 100 c.p.m.

Sample errors for the optimum analysis time of 4 hours were found to be 18%, 10%, and 5% for Th^{232}, U^{238}, and K^{40} respectively. Smaller errors are directly attirbutable to the larger number of net counts occuring in the photopeak. The anticoincidence system effectiveness was evaluated in terms of the ratio $r = R_t/R_b$ and was increased by about 2.5% for all photopeaks when anticoincidence was used. Thus, while the integrated background in the region of 0.1 to 3 MeV was reduced 14% by the anticoincidence system, most of the reduction occurred at 0.15 MeV, and smaller reductions resulted

at the measured photopeak energies. Detection limits for U^{238} and Th^{232} were improved by an order of magnitude when compared to the earlier measurements of Hurley and Adams.

REFERENCES

Adams, J.A.S., Richardson, J.E., and Templeton, C.C. (1958): *Geochimica et Cosmochimica Acta 13*, 270.

Adams, J.A.S., and Gasparini, P. (1970): Gamma-Ray Spectrometry of Rocks, Elsevier.

Arya, A.P. (1966): Fundamentals of Nuclear Physics, Allyn and Bacon Inc.

Bertini, H.W. and Dresner, L. (1962): ORNL-3383, Neutron Physics Division, Oak Ridge National Laboratory.

Bevington, P.R. (1969): Data Reduction and Error Analysis for the Physical Sciences, McGraw-Hill.

Birch, F. (1954): Nuclear Geology, Chap. 5, (Edited by H. Faul), Wiley.

Birks, J.B. (1964): Theory and Practice of Scintillation Counting, Pergamon Press.

Block, F. (1928): *Z. Phys 52*, 555.

Bowen, T. (1954): *Phys. Rev. 96*, No. 3, 754.

Carmichael, H. (1957): *Phys. Rev. 107*, 1401.

Chiang, H.H. (1969): Basic Nuclear Electronics, Wiley-Interscience.

Crouthamel, C.E. (1970): Applied Gamma-Ray Spectrometry, Pergamon Press.

Delaney, C.F.G. (1969): Electronics for the Physicist, Penguin Books Inc.

Delibrias, G. and Repaire, J.L. (1967): "Radioactive Dating and Methods of Low Level Counting," International Atomic Energy Agency, pp. 603-611.

De Voe, J.R. (1961): Nuclear Science Series Report No. 34, National Academy of Sciences, National Research Council Publication 895.

Faul, H. (Ed.) (1954): Nuclear Geology, Wiley.

Ginzburg, V.L. (1969): The Astrophysics of Cosmic Rays, Keter Press.

Grinberg, B. and Le Gallic, Y. (1961): *Intl. J. Appl. Rad. and Isotopes 12*, 104.

Grodstein, W.R. (1957): Natl. Bur. Std., Circ. 583.

Heath, R.L. (1964): Scintillation Spectrometry, U.S. Atomic Energy Commission.

Hultqvist, B. (1956): *Kungl. Svenska Vetenskopokadenisans Handlingar 6*, No. 3.

Hurley, P.M. (1956): *Bull. Geol. Soc. Amer. 67*, 395.

Jackson, J.D. (1956): *Can. J. Phys. 34*, pp. 767-779.

Koczy, F.F. (1954): Nuclear Geology (Ed. H. Faul), Chap. 2.4C, Wiley.

Landau, L. (1944): *J. Phys. (U.S.S.R.), 8*, 201.

Lowder, W.M., and Solon, L.R. (1956): U.S. Atomic Energy Commission Report NYO-4712.

Marinelli, Miller, May, and Rose (1961): Advances in Biological and Medical Physics, Vol. VIII, Academic Press.

May, H., and Marinelli, L. (1961): Argonne National Laboratory, Preprint for Vienna Symposium of International Atomic Energy Commission.

May, H., and Steingraber, O.J. (1958): Argonne National Laboratory Report ANL-5967, 145.

McCall, R.C. (1960): *Health Physics 2*, 304.

Nielsen, J.M. and Perkins, R.W. (1967): "Radioactive Dating and Methods of Low Level Counting," International Atomic Energy Agency, Vienna, pp. 687-702.

O'Brien, K. (1972): "The Cosmic Ray Field at Ground Level," Second International Symposium on the Natural Radiation Environment, Houston, Texas.

Olsen, C.A. and Spencer, L.V. (1958): *J. Res. Nat. Bur. Standards 60,* 85.

Perkins, R.W., Nielsen, J.M., and Diebel, R.N. (1960): *The Review of Scientific Instruments 31,* 1344.

Peters, B. (1958): Handbook of Physics, Chap. 9, (Ed. E.U. Condon and H. Odishaw), McGraw-Hill.

Pine, J., Davisson, R.J., and Greisen, K. (1959): *Nuovo Cimento, Ser. IX,* 14, 1181.

Plano, R.J. (1960): *Phys. Rev. 119,* 1400.

Rockwell, T. (Ed.) (1956): Reactor Shielding Design Manual, McGraw-Hill.

Rossi, B. (1948): *Rev. Mod. Phys. 20,* 537.

Rossi, B. (1952): High Energy Particles, Prentice-Hall Inc.

Roulston, K.I. and Naqvi, S.I. (1957): *Nucleonics 15,* 10, 86.

Rybach, L., von Raumer, J., and Adams, J.A.S. (1966): *Pure and Applied Geophysics 63,* 153.

Shafroth, S.M. (1967): Scintillation Spectrometry of Gamma Radiation, Gordon and Breach Science Publishers.

Sharpe, J. (1955): Nuclear Radiation Detectors, John Wiley.

Seitz, F. (1938): *J. Chem. Phys. 6,* 150.

Stenberg, A., and Olsson, I.U. (1968): *Nuclear Instruments and Methods 61,* 125.

Sternheimer, R.M. (1953): *Phys. Rev. 91*, 256.

von Hippel, A. (1936): *Z. Phys. 101*, 680.

Wilson, R.R. (1952): *Phys. Rev. 86*, 261.

APPENDIX I

COMPUTER PROGRAM FOR

CONCENTRATION CALCULATIONS

CONCEN TRACE CDC 6400 FTN V3.0-P355 OPT=0 74/09/18. 1

```
      PROGRAM CONCEN (INPUT,OUTPUT,TAPE5=INPUT,TAPE6=OUTPUT)
      DIMENSION SP(2,23)
      DIMENSION SU(2,18)
      DIMENSION STH(2,19)
C     SAMPLEPARAM ARE T, SM, SN
C     CHANNEL NUMBERS ARE L,M,N
      WRITE(6,100)
100   FORMAT(1H1,1X,*GCOS 1300-2 T=14400  SM=385 WITH AC*,//)
      TBPC=14400.
      T=14400.
      SM=385.
      L=17
      M=10
      N=19
      PHOTOPEAK PARAM ARE DECAY CONSTANTS
      PL=1.70E-17
      BIL=5.86E-4
      UL=4.88E-18
      TLL=3.73E-3
      THL=1.58E-18
C     INTENSITY AND GEOM EFFIC FACTORS
      GPDHP=130.81
      GBIDHBI=22.94
      GTLDHTL=100.21
      READ(5,10) (SP(2,I),I=1,L)
      READ(5,10) (SP(1,I),I=1,L)
10    FORMAT(10F6.0)
2     CONTINUE
      PN=0
      ASP1C=ASP2C=0
      DO 25 I=1,L
      ASP1C=ASP1C+SP(1,I)
      ASP2C=ASP2C+SP(2,I)
      DIFFP=SP(1,I)-SP(2,I)
25    PN=PN+DIFFP
      WRITE(6,101)ASP1C,ASP2C,PN
101   FORMAT(*0*,1X,*TOTAL COUNTS IN K-40 PHOTOPEAK IS ASP1C=*,F6.0,/,
     **BACKGROUND COUNTS IN PHOTOPEAK IS ASP2C=*,F6.0/,
     **NET COUNTS IN PHOTOPEAK IS PN=*,F6.0)
      VSC=5.
      RPC=ASP1C/ASP2C
      RBPC=ASP2C/TBPC
      PNTC=((100./VSC)**2)*((RPC**.5+1.)/(RPC-1.)**2)*RPC**1.5
      PNBC=PNTC/RPC**1.5
      TSPC=((100./VSC)**2)/(RBPC*(1.+1./RPC**.5)*(RPC**.5 -1.)**2)
      TBPC=TSPC/RPC**.5
      TTOTPC=((100./VSC)**2)/(RBPC*(RPC**.5 -1.)**2)
      WRITE(6,200)RPC,RBPC,PNTC,PNBC,TBPC,TSPC,TTOTPC
200   FORMAT(*0*,1X,
     **TOTAL-TO-BACKGROUND RATIO IN K-40 PHOTOPEAK IS RPC=*,E12.5,/,
     **BACKGROUND COUNTING RATE IN COUNTS PER SECOND IS RBPC=*,E12.5,/,
     ** REQUIRED TOTAL COUNTS IS PNTC=*,E8.0,/,
     ** REQUIRED BACKGROUND COUNTS IS PNBC=*,F8.0,/,
     **MINIMUM BACKGROUND COUNTING TIME IN SECONDS IS TBPC=*,F6.0,/,
     **MINIMUM SAMPLE COUNTING TIME IN SECONDS IS TSPC=*,F6.0,/,
```

```
CONCEN    TRACE                    CDC 6400 FTN V3.0-P355 OPT=0   74/09/18. 10
     **MINIMUM TOTAL TIME FOR SAMPLE AND BACKGROUND   IS TTOTPC=*,F6.0)
      PPP=(PN/T)/PL
      CPPP=PPP*SPDHP
      AP40=CPPP*(1.7E-24)*40.
      AP39=AP40/(1.18E-4)
      CP39=AP39/SM
      SPN=(ASP1C+ASP2C)**.5
      SPPP=(SPN/T)/PL
      SCPPP=SPPP*SPDHP
      SAP40=SCPPP*(1.7E-24)*40.
      SAP39=SAP40/(1.18E-4)
      SCP39=SAP39/SM
      VSP=100.*SCP39/CP39
      WRITE(6,26)CP39,SCP39,VSP
      FORMAT(*0*,1X,*CONCENTRATION  OF K-39 IN GM/GM IS CP39=*,E12.5,/,
     ** STANDARD DEVIATION OF CONCENTRATION IN GM/GM IS SCP39=*,E12.5,/,
     ** SAMPLE PER CENT ERROR OF K-39 CONCENTRATION IS VSP=*,E12.5)
      UCONC NEXT
      READ(5,30)(SU(2,I),I=1,M)
      READ(5,30)(SU(1,I),I=1,M)
30    FORMAT(10F6.0)
      CONTINUE
      BIN=0
      ASU2C=ASU2C=0
      DO 35 I=1,M
      ASU1C=ASU1C+SU(1,I)
      ASU2C=ASU2C+SU(2,I)
      DIFFU=SU(1,I)-SU(2,I)
      BIN=BIN+DIFFU
      WRITE(6,102)ASU1C,ASU2C,BIN
102   FORMAT(*0*,1X,*TOTAL COUNTS IN BI-214 PHOTOPEAK IS ASU1C=*,F6.0,/,
     **BACKGROUND COUNTS IN PEAK IS ASU2C=*,F6.0,/,
     **NET COUNTS IN PEAK IS BIN=*,F6.0)
      TBPC=14400.
      VSC=5.
      RUC=ASU1C/ASU2C
      RBUC=ASU2C/TBPC
      UNTC=((100./VSC)**2)*((RUC**.5 +1.)/(RUC-1.)**2)*(RUC**1.5)
      UNBC=UNTC/RUC**1.5
      TSUC=((100./VSC)**2)/(RBUC*(1.+1./RUC**.5)*(RUC**.5 -1.)**2)
      TBUC=TSUC/RUC**.5
      TTOTUC=((100./VSC)**2)/(RBUC*(RUC**.5 -1.)**2)
      WRITE(6,300)RUC,RBUC,UNTC,UNBC,TBUC,TSUC,TTOTUC
00    FORMAT(*0*,1X,
     **TOTAL-TO-BACKGROUND RATIO IN BI214  PHOTOPEAK IS RUC=*,E12.5,/,
     **BACKGROUND COUNTING RATE IN COUNTS PER SECOND IS RBUC=*,E12.5,/,
     ** REQUIRED TOTAL COUNTS IS UNTC=*,F8.0,/,
     ** REQUIRED BACKGROUND COUNTS IS UNBC=*,F8.0,/,
     **MINIMUM BACKGROUND COUNTING TIME IN SECONDS IS TBUC=*,F8.0,/,
     **MINIMUM SAMPLE COUNTING TIME IN SECONDS IS TSUC=*,F8.0,/,
     **MINIMUM TOTAL TIME FOR BACKGROUND AND SAMPLE IS TTOTUC=*,F8.0)
      PPBI=(BIN/T)/BIL
      CPPBI=PPBI*SBIDHBI
      OU=(BIL/UL)*CPPBI
      AU=OU*(1.7E-24)*238.
```

```
      CU=AU/SM
      SBIN=(ASU1C+ASU2C)**.5
      SPPBI=(SBIN/T)/BIL
      SCPPBI=SPPBI*GBIDHBI
      SOU=(BIL/UL)*SCPPBI
      SAU=SOU*(1.7E-24)*238.
      SCU=SAU/SM
      VSU=100.*SCU/CU
      WRITE(6,36)CU,SCU,VSU
36    FORMAT(*0*,1X,*CONCENTRATION OF U-238 IN GM/GM IS CU=*,E12.5,/,
     ** STANDARD DEVIATION OF CONCENTRATION IN GM/GM IS SCU=*,E12.5,/,
     ** SAMPLE PER CENT ERROR OF U-238 CONCENTRATION IS VSU=*,E12.5)
C     TH CONC NEXT
      READ(5,50)(STH(2,I),I=1,N)
      READ(5,50)(STH(1,I),I=1,N)
50    FORMAT(10F6.0)
5     CONTINUE
      TLN=0
      ASTH1C=ASTH2C=0
      DO 55 I=1,N
      ASTH1C=ASTH1C+STH(1,I)
      ASTH2C=ASTH2C+STH(2,I)
      DIFFTH=STH(1,I)-STH(2,I)
55    TLN=TLN+DIFFTH
      PPTL=(TLN/T)/TLL
      CPPTL=PPTL*GTLDHTL
      OTH=(TLL/THL)*CPPTL
      ATH=OTH*(1.7E-24)*232.
      CTH=ATH/SM
      WRITE(6,103)ASTH1C,ASTH2C,TLN
103   FORMAT(*0*,1X,*TOTAL COUNTS IN TL-208 PHOTOPEAK IS ASTH1C=*,F6.0,/,
     **BACKGROUND COUNTS IN PHOTOPEAK IS ASTH2C=*,F6.0,/,
     **NET COUNTS IN PHOTOPEAK IS TLN=*,F6.0)
      TBPC=14400.
      VSC=5.
      RTHC=ASTH1C/ASTH2C
      RBTHC=ASTH2C/TBPC
      THNTC=((100./VSC)**2)*((RTHC**.5 +1.)/(RTHC -1.)**2)*RTHC**1.5
      THNBC=THNTC/RTHC**1.5
      TSTHC=((100./VSC)**2)/(RBTHC*(1.+1./RTHC**.5)*(RTHC**.5-1.)**2)
      TBTHC=TSTHC/RTHC**.5
      TTOTTHC=((100./VSC)**2)/(RBTHC*(RTHC**.5 -1.)**2)
      WRITE(6,400)RTHC,RBTHC,THNTC,THNBC,TBTHC,TSTHC,TTOTTHC
400   FORMAT(*0*,1X,
     **TOTAL-TO-BACKGROUND RATIO IN TL/208 PHOTOPEAK IS RTHC=*,E12.5,/,
     **BACKGROUND COUNTING RATE IN COUNTS PER SECOND IS RBTHC=*,E12.5,/,
     ** REQUIRED TOTAL COUNTS IS THNTC=*,F8.0,/,
     ** REQUIRED BACKGROUND COUNTS IS THNBC=*,F8.0,/,
     **MINIMUM BACKGROUND COUNTING TIME IN SECONDS IS TBTHC=*,F8.0,/,
     **MINIMUM SAMPLE COUNTING TIME IN SECONDS IS TSTHC=*,F8.0,/,
     **MINIMUM TOTAL TIME FOR BACKGROUND AND SAMPLE IS TTOTTHC=*,F8.0)
      STLN=(ASTH1C+ASTH2C)**.5
      SPPTL=(STLN/T)/TLL
      SCPPTL=SPPTL*GTLDHTL
      SOTH=(TLL/THL)*SCPPTL
```

```
      SATH=SOTH*(1.7E-24)*232.
      SCTH=SATH/SM
      VSTH=100.*SCTH/CTH
      WRITE(6,56)CTH,SCTH,VSTH
   56 FORMAT(*0*,1X,*CONCENTRATION OF TH-232 IN GM/GM IS CTH=*,E12.5,/,
     ** STANDARD DEVIATION OF CONCENTRATION IN GM/GM IS SCTH=*,E12.5,/,
     ** SAMPLE PER CENT ERROR OF TH-232 CONCENTRATION IS VSTH=*,E12.5)
      RTHU=CTH/CU
      WRITE(6,58)RTHU
   58 FORMAT(*0*,1X,*RATIO OF TH-232 TO U-238 IS RTHU=*,E12.5)
      END
```

APPENDIX II

RESULTS OF THE COMPUTER PROGRAM

FOR THE GCOS 1300-2 SAMPLE

```
GCOS 1300-2 T=14400  SM=385 WITH AC


 TOTAL COUNTS IN K-40 PHOTOPEAK IS ASP1C= 6776.
BACKGROUND COUNTS IN PHOTOPEAK IS ASP2C= 4487.
NET COUNTS IN PHOTOPEAK IS PN= 2289.

 TOTAL-TO-BACKGROUND RATIO IN K-40 PHOTOPEAK IS RPC=  .15101E+01
BACKGROUND COUNTING RATE IN COUNTS PER SECOND IS RBPC=  .31160E+00
 REQUIRED TOTAL COUNTS IS PNTC=  6358.
 REQUIRED BACKGROUND COUNTS IS PNBC=  3426.
MINIMUM BACKGROUND COUNTING TIME IN SECONDS IS TBPC=10994.
MINIMUM SAMPLE COUNTING TIME IN SECONDS IS TSPC=13511.
MINIMUM TOTAL TIME FOR SAMPLE AND BACKGROUND  IS TTOTPC=24505.

 CONCENTRATION  OF K-39 IN GM/GM IS CP39=  .26706E-02
STANDARD DEVIATION OF CONCENTRATION IN GM/GM IS SCP39=  .12382E-03
 SAMPLE PER CENT ERROR OF K-39 CONCENTRATION IS VSP=  .46364E+01

 TOTAL COUNTS IN BI-214 PHOTOPEAK IS ASU1C=10666.
BACKGROUND COUNTS IN PEAK IS ASU2C= 9398.
NET COUNTS IN PEAK IS BIN= 1268.

 TOTAL-TO-BACKGROUND RATIO IN BI214  PHOTOPEAK IS RUC=  .11349E+01
BACKGROUND COUNTING RATE IN COUNTS PER SECOND IS RBUC=  .65264E+00
 REQUIRED TOTAL COUNTS IS UNTC=  54869.
 REQUIRED BACKGROUND COUNTS IS UNEC=  45382.
MINIMUM BACKGROUND COUNTING TIME IN SECONDS IS TBUC=  69536.
MINIMUM SAMPLE COUNTING TIME IN SECONDS IS TSUC=  74078.
MINIMUM TOTAL TIME FOR BACKGROUND AND SAMPLE IS TTOTUC= 143614.

 CONCENTRATION OF U-238 IN GM/GM IS CU=  .43501E-06
 STANDARD DEVIATION OF CONCENTRATION IN GM/GM IS SCU=  .48534E-07
 SAMPLE PER CENT ERROR OF U-238 CONCENTRATION IS VSU=  .11171E+02

 TOTAL COUNTS IN TL-208 PHOTOPEAK IS ASTH1C= 1880.
BACKGROUND COUNTS IN PHOTOPEAK IS ASTH2C= 1409.
NET COUNTS IN PHOTOPEAK IS TLN=  471.

 TOTAL-TO-BACKGROUND RATIO IN TL/208 PHOTOPEAK IS RTHC=  .13343E+01
BACKGROUND COUNTING RATE IN COUNTS PER SECOND IS RBTHC=  .37847E-01
 REQUIRED TOTAL COUNTS IS THNTC=  11890.
 REQUIRED BACKGROUND COUNTS IS THNBC=  7715.
MINIMUM BACKGROUND COUNTING TIME IN SECONDS IS TBTHC=  78843.
MINIMUM SAMPLE COUNTING TIME IN SECONDS IS TSTHC=  31072.
MINIMUM TOTAL TIME FOR BACKGROUND AND SAMPLE IS TTOTTHC= 169915.

 CONCENTRATION OF TH-232 IN GM/GM IS CTH=  .21251E-05
 STANDARD DEVIATION OF CONCENTRATION IN GM/GM IS SCTH=  .25876E-06
 SAMPLE PER CENT ERROR OF TH-232 CONCENTRATION IS VSTH=  .12176E+02

 RATIO OF TH-232 TO U-238 IS RTHU=  .48853E+01
```